Construction and Building Materials 544 (2026) 148269

Contents lists available at ScienceDirect

Construction and Building Materials

journal homepage: www.elsevier.com/locate/conbuildmat

Enhanced mechanical property and CO_2 sequestration of low-lime cement via calcium and magnesium nitrates: Cation-dependent effects on carbonation kinetics, crystal development, and pore structure

Seongmin Cho [a], Heongwon Suh [b], Sungwon Sim [c], Jihwan Yang [a], Taiyan Piao [a], Peiqi Li [d], Sungchul Bae [a,*]

[a] Department of Architectural Engineering, Hanyang University, Seoul, 04763, South Korea
[b] Department of Architectural Engineering, Pusan National University, Busan, 46241, South Korea
[c] Central Research Institute, Korea Hydro & Nuclear Power Co., Ltd., Daejeon, 34101, Republic of Korea
[d] Key Laboratory for Green & Advanced Civil Engineering Materials and Application Technology of Hunan Province, College of Civil Engineering, Hunan University, Changsha, 410082, PR China

ARTICLE INFO

Keywords:
Low-lime cement
CO_2-curing
Calcium nitrate ($Ca(NO_3)_2$)
Magnesium nitrate ($Mg(NO_3)_2$)
Calcium carbonate ($CaCO_3$)
Reaction kinetics
Crystal development
Pore refinement

ABSTRACT

Low-lime cement (LLC) is gaining attention as a sustainable binder for CO_2 utilization. However, its slow reaction kinetics often necessitate chemical activation. This paper presents the comparative effects of Ca^{2+} and Mg^{2+} on the phase formation, microstructural evolution, and mechanical performance of CO_2-cured LLC composites. $Ca(NO_3)_2$ and $Mg(NO_3)_2$ were introduced at controlled concentrations to regulate the early ionic environment while maintaining identical anionic conditions. Both additives substantially enhanced the carbonation of LLC, leading to pronounced changes in carbonate formation and pore structure. The addition of $Ca(NO_3)_2$ promoted the formation of a heterogeneous but strongly interlocked microstructure dominated by larger calcite crystals, whereas the addition of $Mg(NO_3)_2$ produced a more uniformly refined microstructure characterized by smaller polyhedral Mg-calcite particles. Reaction kinetic modelling confirmed the characteristic reaction of the LLCs modified by the addition of Ca^{2+} and Mg^{2+}. Consequently, the LLCs activated with a concentration of 0.5 M $Ca(NO_3)_2$ and $Mg(NO_3)_2$ exhibited 2.7 and 2.3 times higher compressive strengths, respectively, than those without activation after 24 h of CO_2-curing. These results demonstrate that the carbonation behavior and strength development of LLCs strongly depend on the type of added cations and highlight the importance of cation selection and concentration control for performance enhancement.

1. Introduction

The cement and concrete sectors account for a substantial share of global anthropogenic carbon dioxide (CO_2) emissions, mainly owing to limestone calcination and energy-intensive clinker production [1–3]. In response to the growing urgency for climate change mitigation, carbon capture, utilization, and storage (CCUS) has emerged as an essential means of addressing unavoidable emissions from cement production [4–8]. Among CCUS technologies applicable to cement-based materials, CO_2-curing has attracted increasing attention as a practical methodology for CO_2 utilization [9–13]. CO_2-curing promotes the reaction between CO_2 and the calcium-bearing phases to form thermodynamically stable calcium carbonate ($CaCO_3$). This leads to the permanent fixation of CO_2 while altering the internal structure of cementitious materials, which is often accompanied by improved early strength and reduced pore volume [9–12,14–16].

Low-lime cement (LLC), mainly composed of non- or low-hydraulic calcium silicate phases (CS, C_3S_2, and C_2S), has emerged as a promising material for CO_2-curing because it requires less $CaCO_3$ and lower calcination temperatures during manufacturing [17–22]. Consequently, LLCs exhibit significantly lower embodied CO_2 than conventional hydraulic cement while retaining sufficient reactivity under CO_2-curing conditions [22,23]. These kinds of materials continue to be actively developed: recent work has extended it to clinkers produced from limestone mining rejects [22] and has examined the reactivity of the constituent calcium silicate phases according to their polymorph [24,25].

* Corresponding author.
E-mail address: sbae@hanyang.ac.kr (S. Bae).

https://doi.org/10.1016/j.conbuildmat.2026.148269
Received 26 April 2026; Received in revised form 7 August 2026; Accepted 17 September 2026
Available online 22 September 2026
0950-0618/© 2026 Elsevier Ltd. All rights are reserved, including those for text and data mining, AI training, and similar technologies.

During carbonation, LLCs can form various $CaCO_3$ polymorphs including calcite, aragonite, and vaterite, whose crystal morphologies and spatial distributions influence pore filling, microstructural densification, and strength development [26,27]. Consequently, the carbonation behavior of LLCs directly governs their mechanical performance and potential as CO_2 sequestering materials [28,29].

Despite these advantages, the limited intrinsic reactivity of calcium silicate in LLCs often results in slow reactions and insufficient $CaCO_3$ formation [30]. In numerous cases, a substantial fraction of the reactant phases in LLCs remains uncarbonated after CO_2-curing, leading to low strength [9,19,20,31–33] and necessitating the use of compression molding with a low water-to-binder ratio [17,31,34,35]. This indicates that the carbonation potential of LLC is not fully utilized and that additional reactivity can be achieved if the chemical environment is appropriately modified.

The chemical environment of the pore solution during the initial LLC reaction strongly influences the extent of Ca dissolution, the precipitation of carbonates, and the resulting pore structure [36–38]. Accordingly, regulating the ionic environment by adding soluble additives during the mixing of LLCs can provide an effective approach for controlling the carbonation and hardening of LLCs [39–41]. In particular, the incorporation of soluble Mg compounds has been reported to significantly improve strength by modifying the carbonation products and refining the microstructure [42–45]. Mg^{2+} exerts powerful effects by interfering with calcite growth and stabilizing amorphous calcium carbonates (ACC) [46–49]. This often results in a favorable precipitation of aragonite or calcite with a distorted crystal lattice structure [42,50,51]. Consequently, Mg^{2+} can alter the crystal morphology and internal microstructure even at low dosages, thereby improving the mechanical properties [43,44,52]. However, previous studies on the incorporation of Mg^{2+} into LLCs have seldom reported an increased degree of carbonation, contrary to the substantial increase in mechanical properties, which is possibly attributed to the inhibition effect of Mg^{2+} [44,45,52]. In addition, the effects of incorporating magnesium compounds into LLC have never been compared with those of incorporating identical amounts of calcium compounds, and it is necessary to distinguish the independent effect of Mg^{2+} from the effect of anions inevitably present in the compound (such as NO_3^- [42], Cl^- [43–45], and SO_4^{2-} [53]).

Providing additional Ca^{2+} in the initial stage has significant potential to increase the carbonation degree of the reactant phases and improve strength through enhanced $CaCO_3$ formation and microstructural densification [28,54]. The supplementation of Ca^{2+} at the initial stage not only provides additional cations that are readily available to form $CaCO_3$, but also further activates the entire reaction by modifying the chemical environment relevant to carbonation. Although the addition of Ca^{2+} in the initial reaction stage may not induce the same morphological modifications of $CaCO_3$ as Mg^{2+}, it can effectively enhance the formation of $CaCO_3$ throughout the reaction. The concentration of Ca^{2+} in the reaction system is also relevant to the formation rate, size, shape, and polymorphs of $CaCO_3$ [37,55,56] while also affecting the dissolution of calcium silicate minerals by interfering with chemical equilibrium [57–60]. Hence, the carbonation of LLCs incorporating soluble calcium compounds is worth investigating in comparison with that of magnesium compounds. Nevertheless, such comparative approaches have not been investigated thus far.

Therefore, this study aimed to investigate the comparative cation-dependent effects of Ca^{2+} and Mg^{2+} during CO_2-curing on the carbonation kinetics and crystal development of LLC. $Ca(NO_3)_2$ and $Mg(NO_3)_2$ were utilized as soluble cation additives. They provide divalent Ca^{2+} and Mg^{2+} while sharing the same NO_3^- counterion, thereby minimizing the differences induced by anion. Both are highly soluble ($Ca(NO_3)_2$:121 g/100 mL H_2O [61] and $Mg(NO_3)_2$:71 g/100 mL H_2O [62]), and their solutions are neutral in terms of pH, which is another critical factor influencing carbonation [39]. Other highly soluble calcium and magnesium additives, such as $CaCl_2$ and $MgCl_2$, were excluded to avoid the potential detrimental effects caused by released Cl^- after dissolution [57,63,64].

In this study, the chemical changes in the reaction system induced by additional Ca^{2+} and Mg^{2+} and their influence throughout the entire process were evaluated. The initial ion leaching and pH were examined, followed by phase formation during CO_2 curing. The physicochemical properties of the reaction products were investigated using quantitative X-ray diffraction (QXRD), thermogravimetric analysis (TGA), ^{29}Si solid-state nuclear magnetic resonance (^{29}Si-NMR) spectroscopy, and scanning electron microscopy (SEM). A reaction kinetics analysis was conducted to identify the effects of the respective cations on the phase formation and morphological evolution at different reaction stages. Nanoscale X-ray computed tomography (X-CT) was performed to quantitatively analyze the microstructural refinement enabled by Ca^{2+} and Mg^{2+}. The mechanical properties and CO_2 uptake capacity, which are the key performance indicators of LLCs, were evaluated to verify and compare the enhancement effects of Ca^{2+} and Mg^{2+} addition. The results of this study identify the additive type and concentration that provided the highest performance under the present experimental conditions while clarifying the underlying mechanisms.

2. Experimental procedures

2.1. Raw materials

The LLC used in this study was synthesized in a kiln (production capacity: 1.5 ton/day) operated at 1250 ℃ (Korea Institute of Limestone & Advanced Materials, South Korea) [65]. The oxide composition of the LLC was determined using X-ray fluorescence spectroscopy (ZSX PRIMUS IV, Rigaku, Japan) (Table 1). The LLC was mainly composed of CaO and SiO_2 with an approximate molar ratio of 1.0, whereas other oxides accounted for less than 1%. The crystallographic compositions of the LLC were examined using X-ray diffraction (XRD) with Rietveld refinement, as shown in Fig. 1(a). The main crystal phases of the LLC were β-belite, rankinite, pseudo-wollastonite, free lime, and crystalline SiO_2 (tridymite, quartz, and cristobalite). Their quantitative values are listed in Table 2. The LLC used in this study consisted of approximately 90% of carbonatable phases (β-belite, rankinite, pseudo-wollastonite, and free lime). The formation of crystalline SiO_2 is inevitable during bulk material production, resulting in the simultaneous synthesis of C_2S and C_3S_2 with Ca/Si ratios greater than 1.0 [66]. The particle size distribution was measured via a laser diffraction analyzer (Mastersizer 3000, Malvern Panalytical, UK) [67], which displayed a distribution with a major hump near the region of 10 μm as shown in Fig. 1(b). The physical properties of the LLC are summarized in Table 3.

To elucidate the effects of $Ca(NO_3)_2$ and $Mg(NO_3)_2$ on the carbonation and strength development of LLC, extra-pure calcium nitrate tetrahydrate ($Ca(NO_3)_2{\cdot}4\,H_2O$, 97%. Daejung Chemicals & Metals Co. Ltd., South Korea) and magnesium nitrate hexahydrate ($Mg(NO_3)_2{\cdot}6\,H_2O$, 98%. Daejung Chemicals & Metals Co. Ltd., South Korea) were pre-dissolved in water to achieve the molar concentrations of 0, 0.1, 0.5, and 1.0 M. The salts were introduced in solution form to avoid transient local changes in temperature and ionic concentration associated with their dissolution during mixing [68–70]. Pre-dissolution also enabled uniform distribution of the additives and accurate control of their molar concentrations from the beginning of the reaction. The mix proportions used in this study are listed in Table 4.

Table 1
Oxide compositions of LLC.

Oxide	Content (%)	Oxide	Content (%)	Oxide	Content (%)
CaO	49.07	**SO_3**	0.01	**K_2O**	0.37
SiO_2	48.34	**MgO**	0.68	**MnO**	0.03
Al_2O_3	0.48	**Cr_2O_3**	0.01	**P_2O_5**	0.06
Fe_2O_3	0.31	**Na_2O**	0.11	**LOI**	0.5

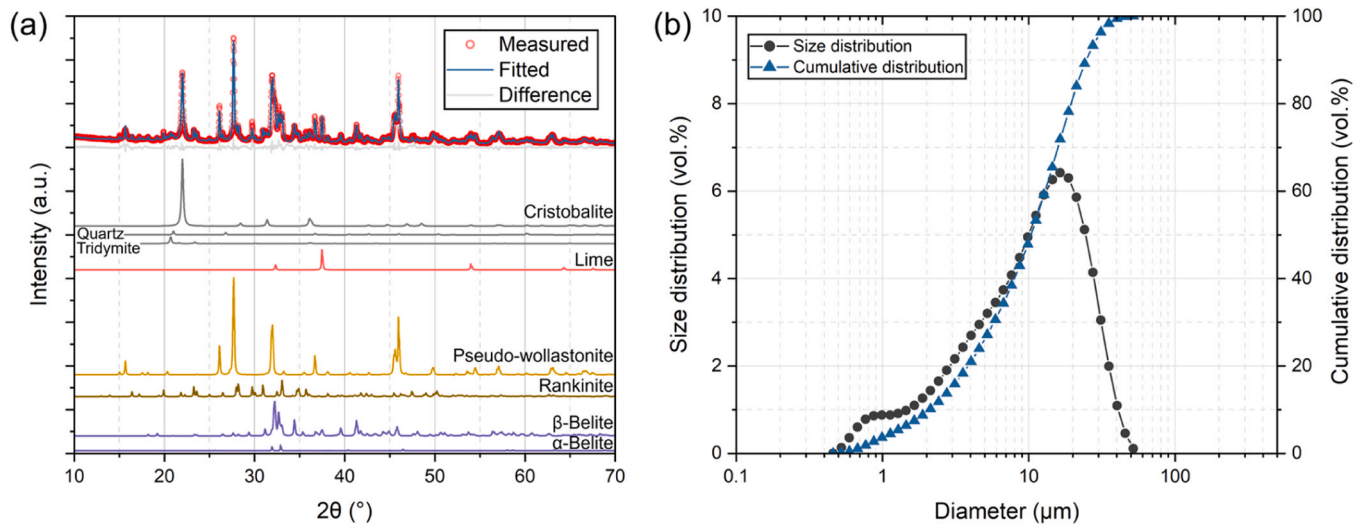

Fig. 1. (a) Refined XRD pattern and (b) particle size distribution of LLC.

Table 2
Crystallographic phase composition of LLC.

Phase	C_2S (α, β-Belite)	C_3S_2 (Rankinite)	CS (Pseudo-wollastonite)	CaO (Free lime)	SiO_2 (Cristobalite, Quartz, Tridymite)
Content	28.05	19.16	40.15	1.86	10.78

*Determined by XRD-Rietveld refinement, Rap= 8.54

Table 3
Physical properties of LLC.

Density	BET-specific surface area	Particle size D_{10}	Particle size D_{50}	Particle size D_{90}
2.81 g/cm^3	0.981 m^2/g	2.38 μm	11.8 μm	28.1 μm

2.2. Sample preparation procedures

Samples were prepared according to the procedure shown in Fig. 2. The LLC was mixed with the nitrate solutions at a liquid-to-solid ratio (L/S) of 0.4, followed by casting into 5 × 5 × 10 mm stainless-steel molds (Fig. 2(a)) [28,29,71–74]. Although the L/S ratio was fixed at 0.4, the effective initial water-to-LLC ratio varied because the mass fraction of the nitrate salt increased with increasing molar concentration of the mixing solution. The calculated effective initial water-to-LLC ratios are also presented in Table 4. The relatively small specimen dimensions were selected to minimize macroscopic CO_2 diffusion limitations, allowing the influence of cation type and concentration on the intrinsic carbonation behavior of LLC to be evaluated independently of specimen scale.

The samples were demolded after pre-curing in an oven at 60 ℃ (Fig. 2(b)). This pre-curing procedure enabled an easier molding of the samples with high L/S while encouraging strength development by modulating the moisture content [29,75–77]. The residual free water content after pre-curing was measured for each mixture according to the Eq. (A1) and displayed in Fig. A1 [29]. The samples were weighted after pre-curing and stored in a 105 ℃ dry oven at for additional 24 h to determine the absolute dry weight. The residual water content was approximately 18% and generally decreased to approximately 16% with increasing nitrate concentration. This reduction in water content was small enough compared to the variables of previous studies investigated the effects of water-to-solid ratio (W/S) [78–81], considering that W/S of 0.22 corresponds to 18% of water content (Control) and W/S of 0.19 is identical to 15.9% of water content (C 1.0 and M 1.0). Moreover, the differences between the samples activated by identical concentration of $Ca(NO_3)_2$ and $Mg(NO_3)_2$ were relatively small. The condition immediately after pre-curing and before CO_2 exposure was defined as t = 0 h for the phase evolution analysis. CO_2-curing was performed for 3, 6, and 24 h in a pressure chamber (Phosentech, South Korea). The chamber was initially at atmospheric pressure (0 bar gauge) and was pressurized to 1.0 bar gauge using 99.9% pure CO_2. Based on the partial pressure, the nominal CO_2 concentration was approximately 50 vol% (Fig. 2(c)) [29]. The relative humidity inside the chamber was continuously monitored and maintained above 80% during curing.

To prepare the samples for the investigation of the single-particle reaction (reaction kinetics and SEM), the pre-cured samples were crushed into particles with a thickness smaller than 1 mm and spread

Table 4
Mix proportions of LLC pastes incorporating $Ca(NO_3)_2$ and $Mg(NO_3)_2$.

Sample name	Control	C 0.1	C 0.5	C 1.0	M 0.1	M 0.5	M 1.0
LLC (g)	100						
Mixing solution (g)	40						
L/S	0.4						
Type of mixing solution	Distilled water	$Ca(NO_3)_2$ solution			$Mg(NO_3)_2$ solution		
Concentration (M)	0	0.1	0.5	1.0	0.1	0.5	1.0
Effective W/C	0.4	0.387	0.369	0.342	0.394	0.371	0.345

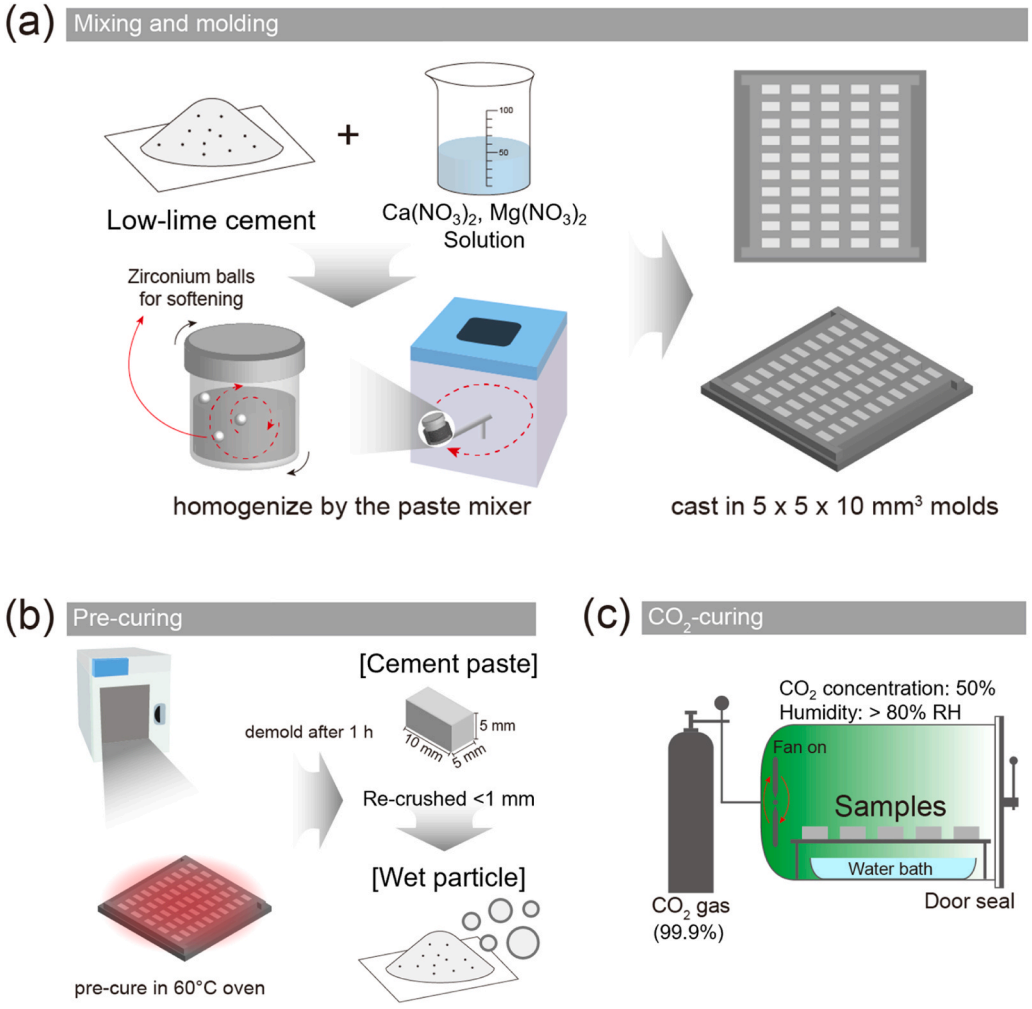

Fig. 2. Schematic of the experimental procedure. (a) Mixing and molding, (b) pre-curing, and (c) CO_2 curing.

uniformly, followed by the same CO_2-curing regime, as shown in Fig. 2 (c). The CO_2-curing of the particle samples was conducted until 168 h when the reaction converged. After CO_2-curing, the samples were immersed in isopropyl alcohol to arrest further reactions [82]. Isopropyl alcohol was renewed twice to accelerate the solvent exchange [83]. Finally, the samples were dried until reaching a constant weight.

2.3. Characterization and analysis

2.3.1. Mechanical property

The compressive strength of LLC blocks was measured through a Microtester (Maximum load: 5 kN, Deben, UK) specialized for investigating the mechanical properties of small samples [84–86]. Uniaxial loading at a rate of 0.03 mm/min was applied to a 5 × 5 mm cross-section of the cuboid sample (5 × 5 × 10 mm) until fracture. More than seven samples were tested to ensure a sufficient representation of variations and improve the reliability and repeatability of the results.

2.3.2. Initial pore solution analysis

The leachates extracted from the fresh LLC paste were analyzed to investigate the initial reaction of the LLC prior to CO_2-curing. After mixing the LLC with the respective nitrate solutions at an L/S ratio of 0.4, the slurry was centrifuged at 4000 rpm for 5 min (Centrifuge 406, LaboGene, Denmark) to separate the supernatant. The extracted supernatant was filtered to remove residual solid particles, yielding a clear solution for analysis. The initial leached Ca^{2+} concentration in the pore solution was measured using inductively coupled plasma optical emission spectrometry. The pH of each solution was determined using a probe-type pH meter (SevenCompact S220; Mettler Toledo, Switzerland).

2.3.3. Quantitative phase analysis

Significant amounts of amorphous phases, including ACC and Ca-modified silica gels, are known to form during carbonation of LLC. To achieve accurate phase quantification, TGA and XRD-Rietveld refinement with an internal standard were employed. The samples used for phase quantification were crushed and finely ground to pass through a 75 μm standard sieve.

TGA was performed over a temperature range of 20–1000 ℃ using a thermogravimetric analyzer (STA7200, HITACHI, Japan) under N_2 purging at a rate of 200 mL/min [87,88]. In CO_2-cured LLCs, the thermal decomposition of carbonates typically initiates at approximately 300 ℃, as evidenced by TGA-mass spectrometry [34,89]. Based on this behavior, the amount of thermally released CO_2 and the corresponding $CaCO_3$ content were estimated using Eqs. (1) and (2), as follows:

$$W_{CO_2} = W_{300℃} - W_{830℃}, \tag{1}$$

$$W_{CaCO_3} = W_{CO_2} \times \frac{M_{CaCO_3}}{M_{CO_2}}, \tag{2}$$

where W_{CaCO_3} and W_{CO_2} denote the amounts of $CaCO_3$ and CO_2 determined by TGA, respectively. $W_{300℃}$ and $W_{830℃}$ are the weight fractions

of samples during TGA at 300 ℃ and 830 ℃, respectively. M_{CaCO_3} and M_{CO_2} are the molar masses of $CaCO_3$ and CO_2, respectively.

The weight gain associated with the formation of the reaction products, including H_2O and CO_2, was determined from the total weight loss measured by TGA, as expressed in Eq. (3).

$$W_{bound} = W_{20℃} - W_{830℃}, \tag{3}$$

where W_{bound} denotes the amount of chemically bound H_2O and CO_2 gained during the reaction, and $W_{20℃}$ and $W_{830℃}$ are the weight fractions of the samples during TGA at 20 ℃ and 830 ℃, respectively.

XRD samples were prepared by homogenizing finely ground samples with ZnO (zincite, Sigma Aldrich, US) as an internal standard [90,91]. The mixing ratio of the sample with ZnO was 4:1 by weight. XRD was performed using a powder diffractometer (D2 Phaser, λ=1.54 Å, Cu-Kα source, Bruker, US) over a 2θ range of 6°–70° with a step size of 0.02° [92]. The constituent crystalline phases were quantitatively identified using DIFFRAC.EVA 4.1 (Bruker, US), and phase compositions were determined by Rietveld refinement using TOPAS 5.0 (Bruker, US). All Rietveld refinements converged with R_{wp} values below 8.68, and the corresponding values are summarized in Table A1. The contents of the crystalline phases were corrected based on the amount of the internal standard, according to Eq. (4). The amorphous phase content was calculated as the amorphous or crystalline phase non-quantified (ACn) using Eq. (5) [82,93].

$$Corr(W_i) = W_i \frac{STD_{known}}{STD_{measured}}, \tag{4}$$

$$W_{ACn} = 1 - \sum_{i=1}^{n} Corr(W_i), \tag{5}$$

where W_i and $Corr(W_i)$ are the weight fractions of the ith crystalline phase before and after the correction with an internal standard, respectively. STD_{known} and $STD_{measured}$ are the known weight fraction of the incorporated internal standard (20% ZnO in this study) and the weight fraction of the internal standard calculated by Rietveld refinement, respectively. W_{ACn} denotes the weight fraction of ACn.

The phase evolution of the LLCs was expressed per unit weight of the binder by applying Eq. (6) [82] considering the weight gain during CO_2-curing.

$$W_{R,i} = \frac{Corr(W_i)}{1 - W_{bound}}, \tag{6}$$

where W_{bound} denotes the amount of chemically bound H_2O and CO_2 as determined by Eq. (3), and $Corr(W_i)$ denotes the weight fraction of the ith crystalline phase as determined by Eq. (4). $W_{R,i}$ denotes the weight fraction of the ith crystalline phase, considering the weight gain.

To assess the reactivity of the LLCs after CO_2-curing, the degree of reaction (DoR) was calculated by comparing the amounts of the constituent reactants before and after the reaction, as shown in Eq. (7) [29]:

$$DoR(t) = \frac{\sum_j R_{r,i,raw} - \sum_j R_{r,i}(t)}{\sum_j R_{r,i,raw}}, \tag{7}$$

where $\sum_j R_{r,i,raw}$ and $\sum_i R_{r,i}(t)$ denotes the summation of the rescaled weight fraction of the ith phase in raw LLC and after a specific CO_2-curing time, respectively.

^{29}Si NMR spectra were obtained using a 500 MHz solid-state NMR spectrometer (Bruker Avance III HD, US) operating at a spinning speed of 7 kHz to investigate the polymerization of the Ca-modified silica gel phases generated after CO_2-curing. A 4 mm cross-polarization magic angle spinning probe was used for ^{29}Si-NMR spectroscopy. The collected chemical shifts of ^{29}Si were referenced to octakis (trimethylsiloxy) silsesquioxane (Q8M8) at 11.5 ppm. Gaussian deconvolution was performed to quantitatively analyze the polymerization of the Si chain structure. The signals were separated into five regions (Q^0–Q^4), corresponding to the chemical shifts of the Si chain structures typically found in cementitious materials [26,94–96].

2.3.4. Reaction kinetics

A gas–solid reaction kinetic model was adopted to describe the reaction progress of single particles [30,97–99]. The reaction was divided into three stages based on the changes in the reaction rate. Stage I corresponds to a rapid initial reaction controlled by progress at the reactive phase boundaries [100]. Stage II represents the transitional regime in which the reaction at the boundary slows. Stage III is characterized by a markedly reduced reaction rate governed by diffusion through the product layers formed during carbonation. The conversion rate, denoted as α (which corresponds to the DoR in this study), was evaluated using the generalized kinetic expression given in Eq. (8), to determine the reaction rate parameters [97]. The apparent reaction rate constant and reaction order were obtained by fitting the logarithmic form of the equation, expressed as Eq. (9):

$$[1 - (1 - \alpha)^{\frac{1}{3}}]^n = kt, \tag{8}$$

$$\ln\left[1 - (1 - \alpha)^{\frac{1}{3}}\right] = \frac{1}{n}\ln(k) + \frac{1}{n}\ln(t), \tag{9}$$

where k is the reaction rate constant, t is the carbonation duration, and n indicates the dominant reaction-controlling step.

2.3.5. Microstructural analysis

The reaction products in the CO_2-cured LLC pastes were observed using field-emission SEM (FE-SEM, JSM 7800 F Prime, JEOL, Japan). To obtain backscattered electron (BSE) SEM images of the internal cross-section, the paste samples were hardened in epoxy resin (EpoFix, Struers, US) and ground using 1200-, 2000-, and 4000-grit silicon carbide abrasive papers, followed by fine polishing using diamond paste on a cloth [101]. Pt was sputtered onto the surface before measurements to ensure electrical conductivity.

High-resolution X-CT was performed to evaluate the spatial distribution and shape characteristics of the pores between the carbonation products quantitatively. The X-CT experiments were conducted at the 7 C X-ray nanoimaging beamline of the Pohang light source (PLS, Pohang, South Korea), operating with a storage beam energy of 3.0 GeV and 300 mA, as shown in Fig. 3 [102]. The samples were shaped into cylindrical cones with diameters smaller than 0.2 mm to ensure the sufficient penetration of incident X-rays into the region of interest. The X-ray energy used for the CT measurement was 9.3 keV. The field of view (FOV) and pixel resolution were approximately 50 μm and 30 nm, respectively. Transmission X-ray images were obtained using a scintillator detector (2048 × 2048, 16 bits, Marana, Andor Technology, UK) (Fig. 3(b)). During image acquisition, the samples were rotated at a speed of 0.5°/s. A total of 1600 transmission images were acquired and reconstructed into a stack image (Octopus 8.1 Reconstruction, TESCAN, Czech Republic) [103]. Spot and ring filters were applied during reconstruction to improve the image quality.

Reconstructed cross-sectional images were processed using Avizo software (Thermo Fisher Scientific, US) [104,105]. As shown in Fig. 3 (c), the reconstructed slices were thresholded based on the grayscale distribution after applying a Gaussian filter to alleviate the noise signals that hinder the segmentation of phases. The binarized pore objects are then divided into separate individual pores. The equivalent diameters (D_{eq}) of the pores were defined and analyzed to assess the size distribution, as shown in Eq. (10), assuming that the pores are spherical.

$$D_{eq} = \sqrt[3]{\frac{6V}{\pi}}, \tag{10}$$

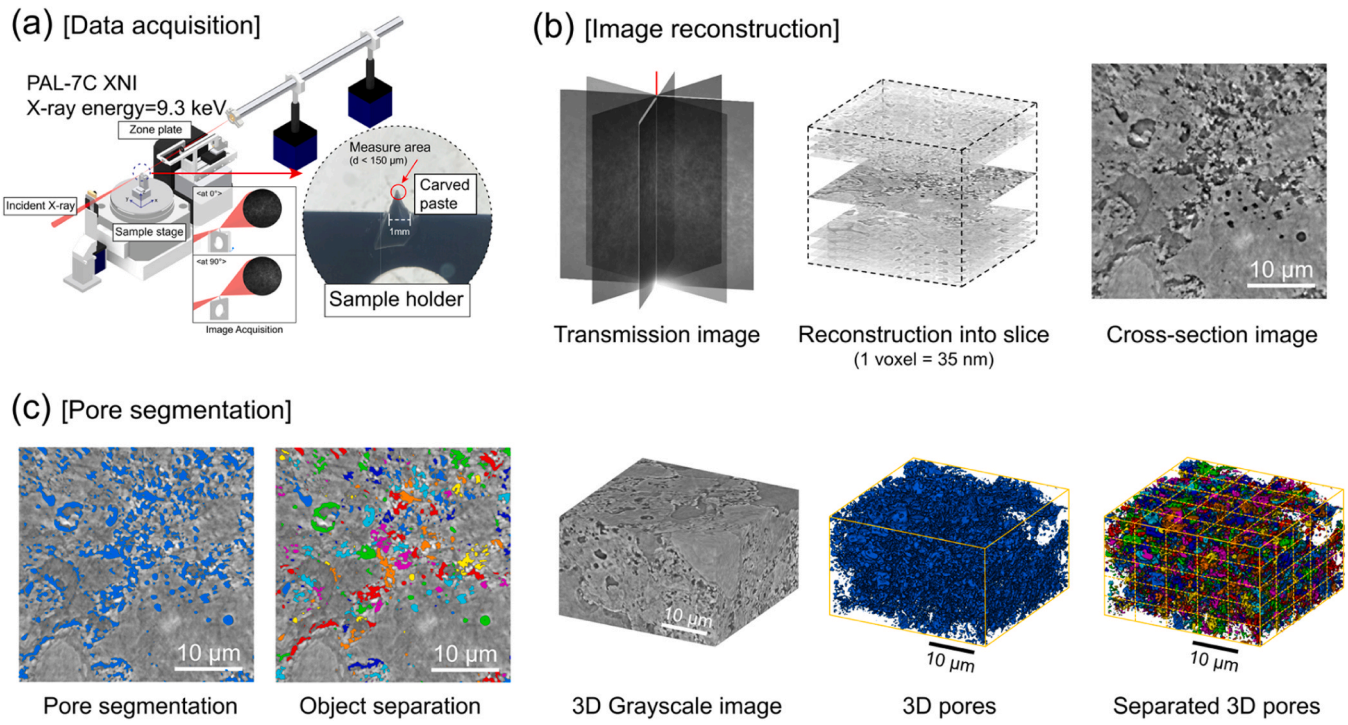

Fig. 3. Schematic of (a) sample preparation and measurement settings of synchrotron X-CT, (b) X-ray transmission image reconstruction, and (c) pore segmentation process.

where V denotes the volume (μm^3) of each pore.

The mechanical behavior of cementitious composites is strongly influenced by both the morphology and spatial arrangement of pores [106–108]. Even at comparable levels of total porosity, variations in pore geometry can lead to noticeable differences in mechanical performance [72,74,108,109]. Irregular pore shapes can intensify the local stress concentrations, thereby affecting the load-bearing capacity. Therefore, the statistical characterization of pore structures has been shown to be an effective approach for capturing the microstructural changes associated with phase evolution in cementitious systems [28,29,71,72,90,110,111].

The spatial distribution of pores was evaluated through the radial distribution function (RDF), which revealed the agglomeration characteristics of the pores, as shown in Fig. 4(a) [106,108]. The pore RDF was determined using Eq. (11).

$$G_r(r) = \frac{\rho_r}{\rho} = \frac{N_r/V_r}{N/V}, \tag{11}$$

where ρ_r, N_r, and V_r represent the mean number density of pores, the number of pores, and volume within a spherical shell of radius r, respectively, whereas ρ, N, and V denote the mean number density, the number of pores, and the volume of the entire sampling region, respectively.

The RDFs were fitted using Eq. (12) to consider the distribution characteristics of pores in typical composites. This fitting equation effectively accounts for the distribution modes of the pores, as depicted in Fig. 4(a).

$$G_r(x) = [G_r(d)] \bullet e^{-\alpha(x-d)^2}, \quad (x < d)$$

$$G_r(x) = 1 + \left[1 - \frac{1}{G_r(d)}\right] \bullet [G_r(d)] \bullet e^{-\gamma(x-d)} \bullet [\mu + (1-\mu) \bullet \cos(\theta \bullet (x-d))], (x \geq d) \tag{12}$$

where x is the dimensionless interpore distance given by r/σ, σ is an adjustable factor used to derive the nondimensional interpore distance, d is the dimensionless distance corresponding to the first peak, $G_r(d)$ is the $G_r(x)$ value of the first peak, α is the rise rate from the origin to the first peak, γ is the decay rate, μ is the oscillation factor beyond the first peak, and θ is the oscillation frequency.

The pore shapes were evaluated using a classification system proposed by Zingg et al. [90,111,112]. Based on the eigenvectors of individual pores, the elongation (I/L) and flatness (S/I) were calculated, as shown in Fig. 4(b), where L, I, and S represent the longest pore dimension, longest dimension perpendicular to L, and shortest dimension perpendicular to the other two axes, respectively. Using these parameters, the pore shapes were categorized as rod-, blade-, cuboid-, plate-, and cube-like according to the Zingg diagram shown in Fig. 4(b), which can effectively classify pores based on their morphological features [74].

3. Results and discussion

3.1. Mechanical performance of activated LLCs

The compressive strengths of the LLCs activated by $Ca(NO_3)_2$ and $Mg(NO_3)_2$ are shown in Fig. 5. For both nitrate activation, a concentration of 0.5 M yielded the highest compressive strength. In the absence of the nitrate additives, the LLCs achieved a compressive strength of 48 MPa after 24 h; however, the addition of 0.5 M $Ca(NO_3)_2$ and $Mg(NO_3)_2$ significantly increased the compressive strength to over 100 MPa, reaching 128 MPa for C 0.5 and 112 MPa for M 0.5. The strength improvement in this study was particularly noteworthy because these strengths were achieved without compression molding, unlike previous studies on LLCs [42,43,47,113–119]. The outstanding mechanical enhancement at 0.5 M was likely attributable to the enhanced reactivity and densified microstructure enabled by proper concentration, with enhanced initial cation availability from the LLCs at the dissolution stage and subsequent crystal development at the precipitation stage. Notably, C 0.5 exhibited a slightly higher compressive strength than M

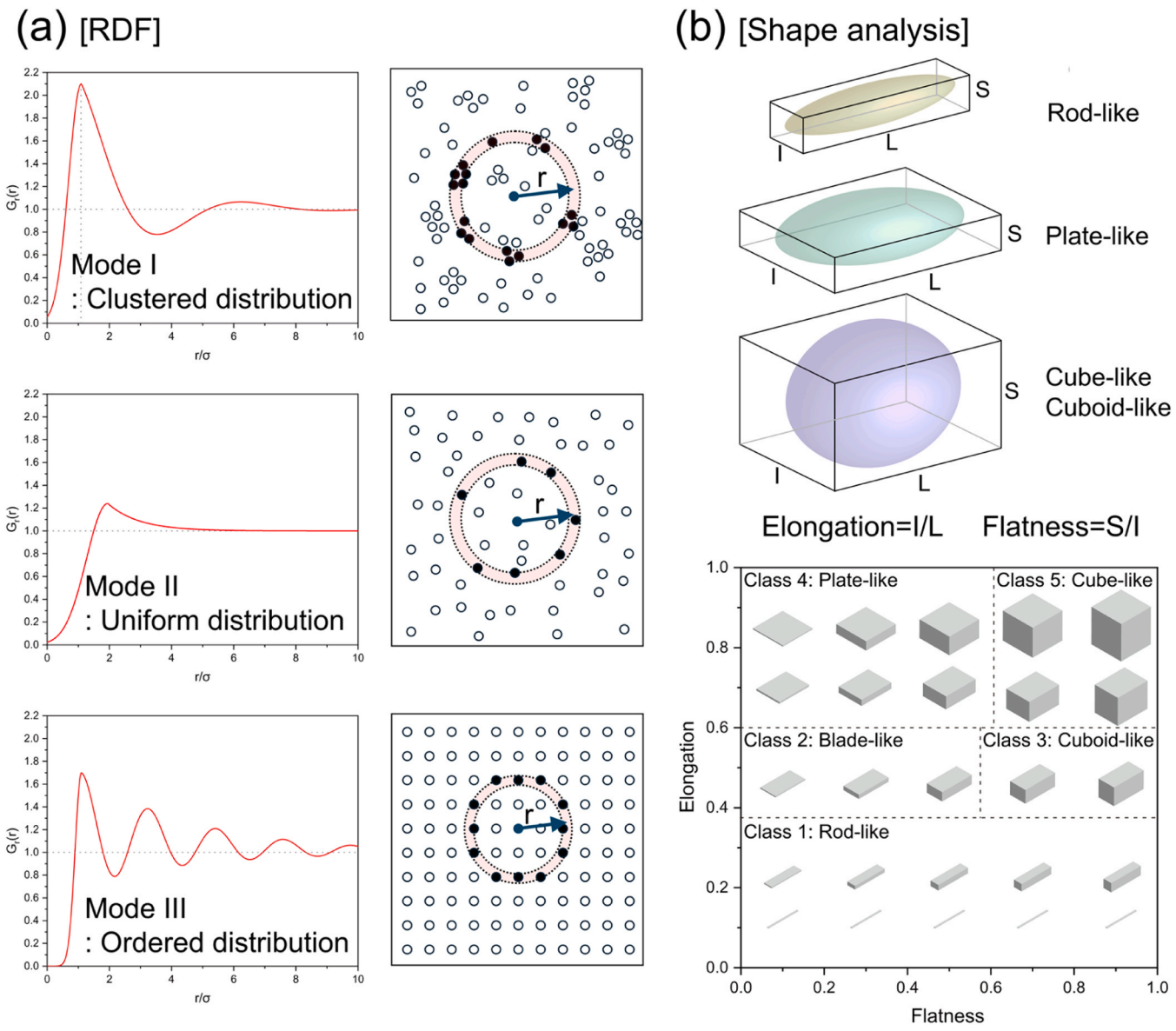

Fig. 4. Pore analysis method using X-CT. (a) Spatial distribution analysis using RDF and (b) pore shape analysis using Zingg's diagram [112].

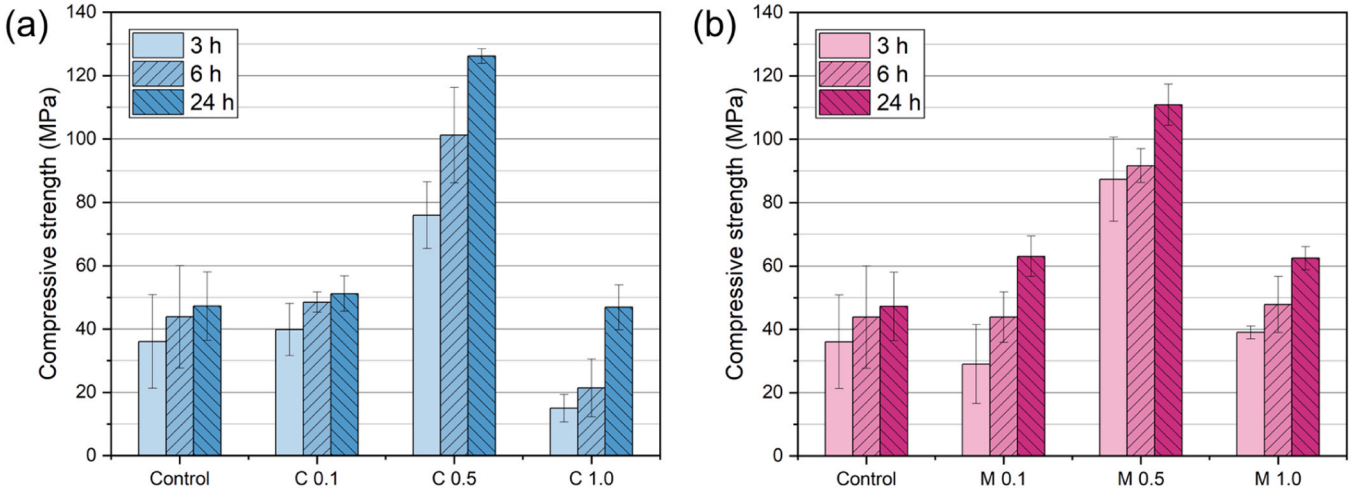

Fig. 5. Compressive strength of the LLCs activated by (a) $Ca(NO_3)_2$ and (b) $Mg(NO_3)_2$.

0.5. This difference can be attributed to the distinct microstructural characteristics of the two samples, which may resulted from the cation-dependent precipitation behavior of the carbonate phases.

Lower (0.1 M) or higher (1.0 M) concentrations of both nitrates resulted in compressive strengths at 24 h that were comparable to or only slightly higher than that of Control. However, different behaviors in the strength development at 3 and 6 h were observed. C 0.1 exhibited slightly higher compressive strength than Control up to 6 h, whereas C 1.0 showed significantly lower strength over at the same period. M 0.1 exhibited lower strength at 3 h; however, this difference was compensated for by 6 h, resulting in a 24 h compressive strength that was 27% higher than that of Control. In contrast, M 1.0 showed slightly higher strength from 3 h onward and achieved a 24 h compressive strength comparable to that of M 0.1. These results demonstrate that the chemical environment modified by nitrate ion and respective cations had a significant influence on carbonation, although an appropriate additive concentration is required to achieve property enhancement. The underlying mechanisms such as phase evolutions and microstructural formation are further discussed in the following sections.

It should be noted that the relatively high absolute compressive strength values obtained in this study were also influenced by the specimen dimensions. The carbonation of LLC is strongly dependent on CO_2 transport from the exposed surfaces into the specimen interior. Therefore, the short CO_2 diffusion distance in the specimens used in this study likely facilitated more extensive and spatially uniform carbonation throughout the cross section during the limited curing period, thereby promoting carbonate precipitation and strength development. In addition, the measured compressive strength may have been influenced by the conventional specimen size effect in testing [120]. Accordingly, the strength values reported herein should primarily be interpreted in terms of the relative differences and trends among the Control and activated samples tested under identical specimen geometries and curing conditions. Direct extrapolation of these absolute values to larger specimens or structural-scale members requires further validation.

3.2. Influences of nitrate solutions on the dissolution of LLCs

Fig. 6(a) shows the concentration of Ca^{2+} leached from the LLCs after mixing with nitrate solutions of varying molarities. The amount of leached Ca^{2+} increased monotonically with increasing concentrations of both $Ca(NO_3)_2$ and $Mg(NO_3)_2$. Notably, $Mg(NO_3)_2$-induced Ca^{2+} leaching was comparable to that of $Ca(NO_3)_2$, demonstrating that the dominant factor governing the increased Ca dissolution is the modification of the electrolytic environment by highly soluble nitrate salts.

Both $Ca(NO_3)_2$ and $Mg(NO_3)_2$ exhibit high solubility; therefore, they completely dissociate in the solution, generating cations and NO_3^-. These dissociated ions act as strong electrolytes, increasing the ionic strength of the reaction system [121,122]. Ionic strength is defined as the sum of the molar concentration and the square of the ionic charge ($\frac{1}{2}\sum c_i z_i^2$) [123]. An increase in ionic strength reduces the apparent activity of Ca^{2+}, thereby shifting the dissolution equilibrium of the calcium silicate phases toward additional Ca^{2+} release. With increasing concentrations of $Ca(NO_3)_2$ and $Mg(NO_3)_2$, the activity coefficient effect became more pronounced, resulting in progressively greater Ca leaching at higher nitrate concentrations. Hence, $Ca(NO_3)_2$ and $Mg(NO_3)_2$ could exert similar effects on Ca^{2+} leaching despite the differences in cation species.

The comparable Ca concentrations obtained with both nitrates indicate that the dissolution was primarily governed by the increase in ionic strength rather than by the direct supply of Ca^{2+} from $Ca(NO_3)_2$. The slightly higher values observed in the LLCs mixed with $Ca(NO_3)_2$, indicated by Δ in Fig. 6(a), can be attributed to the direct supply of Ca^{2+} from the nitrate salt. However, this difference remained relatively small because the increase in Ca^{2+} activity suppressed further dissolution through the common-ion effect [124]. Consequently, the direct Ca^{2+} contribution from $Ca(NO_3)_2$ did not increase the total dissolved Ca to be in proportion to the nitrate concentration.

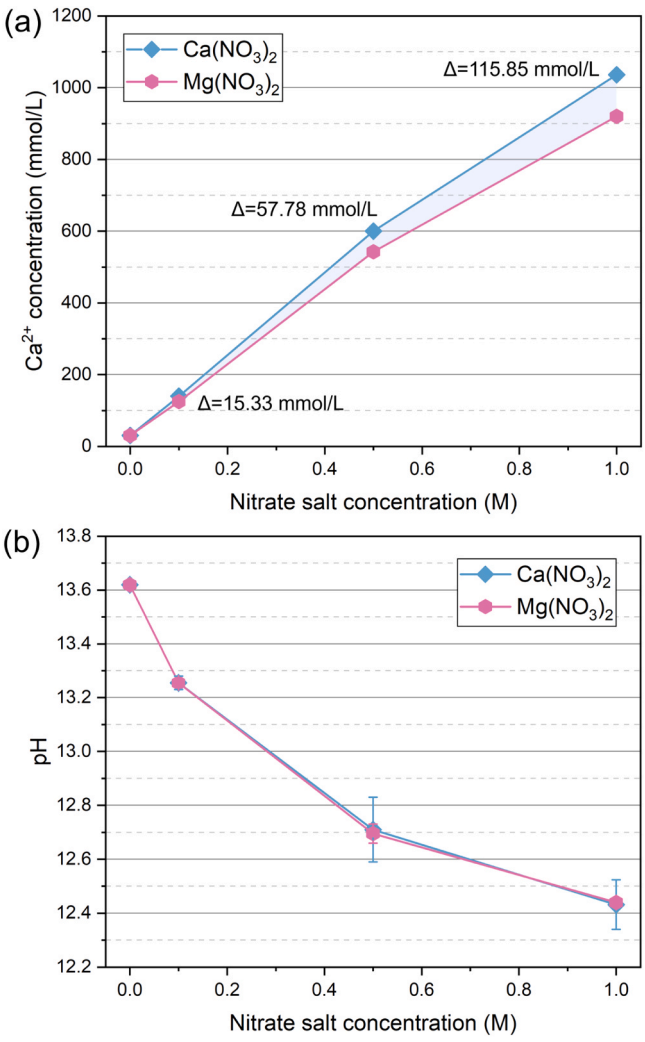

Fig. 6. Initial pore solution analysis of the LLC pastes mixed with nitrate solutions. (a) Ca^{2+} concentration and (b) pH.

The pH values of the leachates are shown in Fig. 6(b). The pH generally decreased with increasing concentrations of both nitrate solutions, regardless of the type of nitrate salt used. Both $Ca(NO_3)_2$ and $Mg(NO_3)_2$ exhibited highly similar pH trends with increasing molar concentrations, indicating that the mechanisms governing the improved dissolution of LLC were similar. Generally, the dissolution of calcium silicate phases during the leaching stage can be described by Eq. (13).

$$Ca_xSi_yO_{(x+2y)} + xH_2O \rightarrow xCa^{2+} + yH_2SiO_4^{2-} + (2x-2y)OH^- \quad (13)$$

According to this equation, an increase in pH could be expected as the dissolution proceeds. Nevertheless, the pH decreased with increasing nitrate concentration, although Ca^{2+} dissolution from the LLC was enhanced. This can be interpreted by considering the formation of ion complexes in alkaline environments. Under alkaline conditions, dissolved Ca can be distributed among free Ca^{2+} and aqueous Ca–OH species, including $CaOH^+$ and $Ca(OH)_2$ (aq) [125,126], according to the following equilibria (Eq. 14):

$$Ca^{2+} + OH^- \rightleftharpoons CaOH^+ \quad (14a)$$

$$Ca^{2+} + 2OH^- \rightleftharpoons Ca(OH)_2 \quad (aq) \quad (14b)$$

The formation of these aqueous species becomes important in the solutions containing Ca, and $Ca(OH)_2$ (aq) has been reported to become a major dissolved Ca species at a high pH of approximately 13 [127]. Furthermore, the substantial increase in ionic strength caused by both nitrate salts alters the activity coefficients of Ca^{2+} and OH^-. Thus, part of the Ca released from the LLC may exist as aqueous Ca–OH species rather than as free Ca^{2+} under the present conditions. Accordingly, the free OH^- activity may not increase in proportion to the total dissolved Ca concentration, resulting in a lower measured pH.

Therefore, enhanced calcium silicate dissolution can increase the total dissolved Ca concentration without a proportional increase in free OH^- activity according to the formation equilibria of aqueous Ca-OH species. Because $Ca(NO_3)_2$ and $Mg(NO_3)_2$ produced comparable increases in Ca dissolution and decreases in pH, this interpretation is

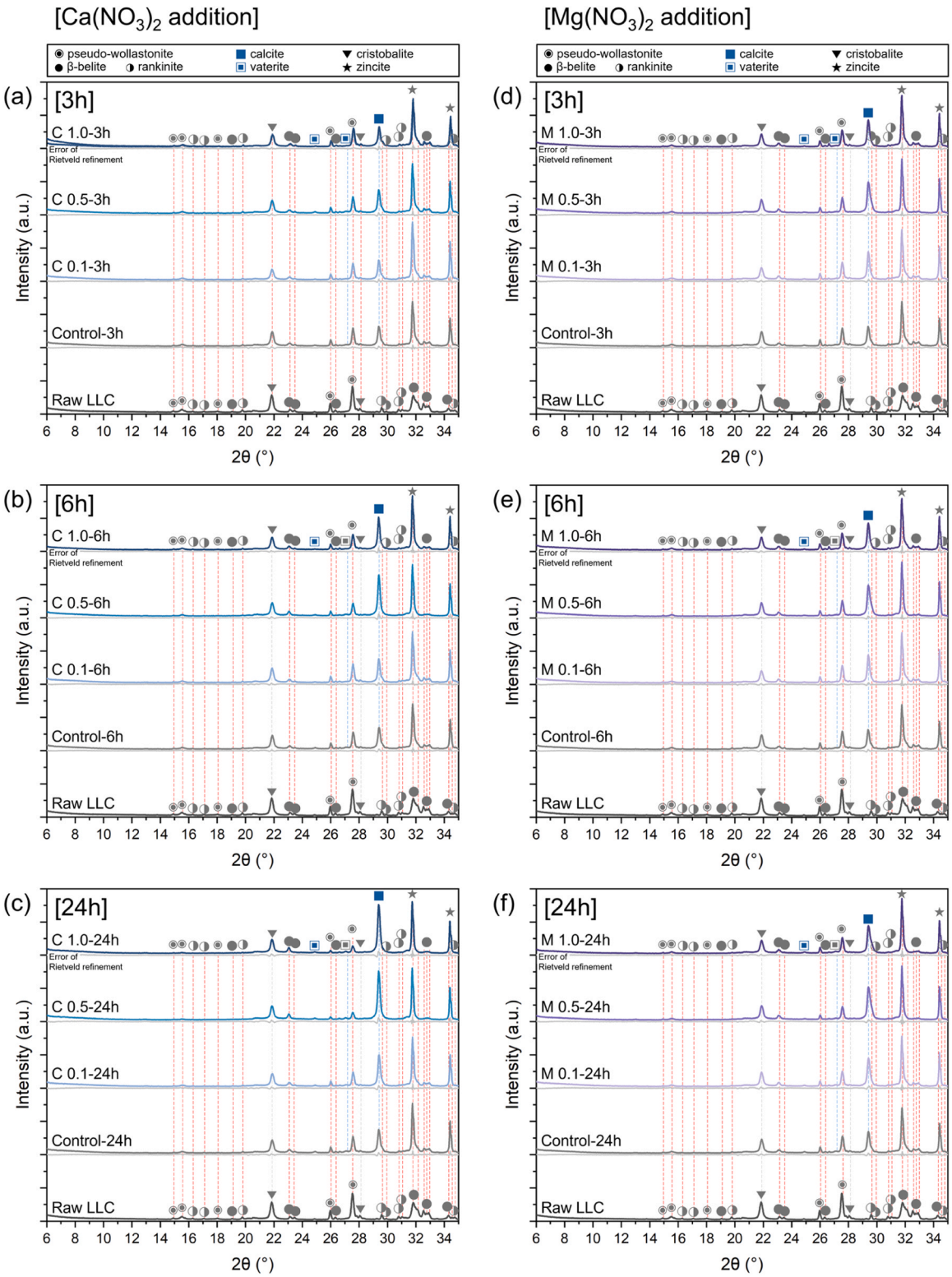

Fig. 7. XRD patterns of the CO_2-cured LLCs activated by nitrate solutions: (a)–(c) $Ca(NO_3)_2$ and (d)–(f) $Mg(NO_3)_2$.

applicable to both cases. Although the individual aqueous Ca species were not directly quantified in this study, the similar trends observed for both nitrate salts support the interpretation based on their effects on ionic strength and Ca-OH speciation.

Greater dissolution of calcium silicates increased the Ca available for subsequent carbonation and could be favorable for strength development. Nevertheless, the dissolved Ca concentration increased continuously with nitrate concentration, whereas the compressive strength reached a maximum at 0.5 M and decreased markedly to 1.0 M. This contrast suggests that Ca release alone did not control the mechanical properties; but also the subsequent phase evolution and pore structure can be the decisive factor.

3.3. Phase evolution of LLCs activated by $Ca(NO_3)_2$ and $Mg(NO_3)_2$

The phase assemblages of the specimens immediately after precuring (before CO_2 exposure) are presented in Fig. A2. No crystalline nitrate salts or other newly formed nitrate-containing phases were identified as shown in Fig. A2 (a) and (b). However, a weak and broad feature appeared near $2\theta = 18^\circ$, corresponding to $Ca(OH)_2$. In Fig. A2 (c) and (d), the quantified crystalline phases are depicted. $Ca(OH)_2$ content ranged from approximately 3.1–4.7 wt%, and the broad diffraction profile indicated its poorly crystalline nature [128–130]. The $Ca(OH)_2$ was likely formed through the hydration of free lime, with a possible minor contribution from β-C_2S during the 1 h treatment at 60 ℃. Despite this limited hydration, no substantial consumption of the

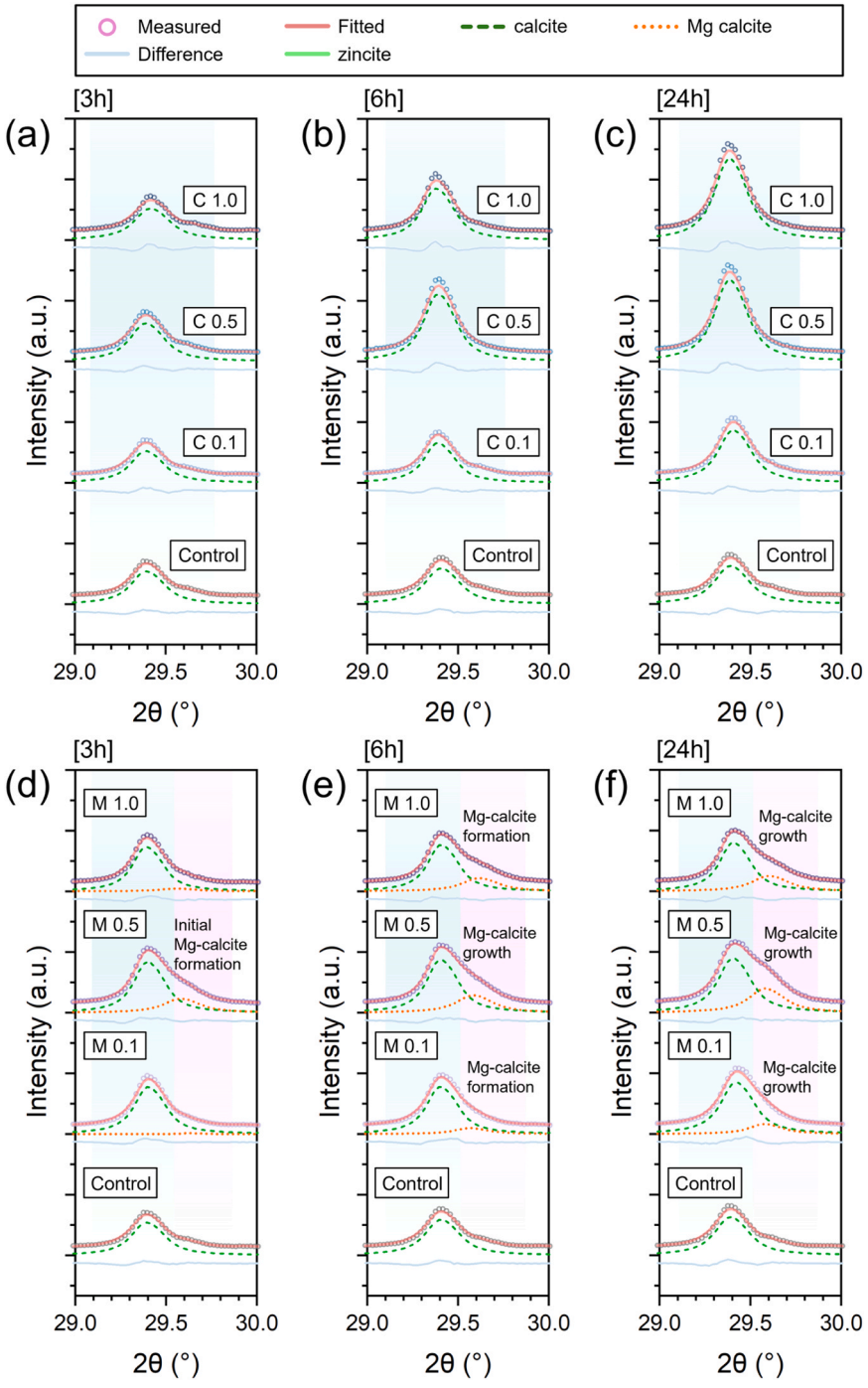

Fig. 8. Refined XRD patterns of the CO_2-cured LLCs activated by (a)–(c) $Ca(NO_3)_2$, and (d)–(f) $Mg(NO_3)_2$ at $2\theta = 29^\circ$–30°.

major calcium silicate phases was observed. The variations in C_2S, C_3S_2, and CS among the pre-cured specimens remained within approximately 1 wt%. The ACn content reached up to approximately 3 wt%, which may include poorly crystalline hydration products formed during pre-curing. Possible nitrate complexation may also contribute to this fraction, although it could not be independently identified by XRD. These results indicate that pre-curing induced limited initial hydration but did not cause considerable reconstruction of the major LLC phases prior to CO_2 exposure.

The refined XRD patterns of the LLC pastes containing $Ca(NO_3)_2$ and $Mg(NO_3)_2$ are shown in Fig. 7. In the 2θ range of 6°–35°, diffraction peaks attributed to the crystallographic planes corresponding to calcite (■), vaterite (▣), pseudo-wollastonite (CS, ◉), rankinite (C_3S_2, ◑), β-belite (C_2S, ●), cristobalite (▼), and zincite (★) were observed. Calcite and vaterite were identified as the main reaction products in all the samples along with CO_2-curing. The crystallographic traces of the other reaction products were scarcely observed. No nitrate-bearing crystalline phase was identified in the XRD patterns.

As the CO_2-curing progressed, the peaks corresponding to CS, C_3S_2, and C_2S gradually decreased, accompanied by an increase in calcite and vaterite intensities. Alterations in the major peaks of the key phases are clarified in the 2θ range of 27°–35°, as shown in Fig. 8 and Fig. 10. Notable differences in the peak intensities of the reactants and products were observed according to the concentrations of $Ca(NO_3)_2$ and $Mg(NO_3)_2$.

Fig. 8 shows the XRD patterns in the 2θ region of 29°–30°, where the diffraction by the main peak of calcite (1 0 4 plane) is observed. After 3 h of CO_2-curing, the growth of the calcite peak (at 2θ=29.5°) was subtle in the samples mixed with $Ca(NO_3)_2$ (Fig. 7(a)–(c)), with only C 0.5 presenting a distinguishable increase in the peak intensity of calcite. After 6 h, the differences between the samples with different molar concentrations of $Ca(NO_3)_2$) became distinct. In Fig. 8(b) and (c), C 0.5 showed the highest increase in the calcite peak. C 1.0 and C 0.1 also showed a slight increase in the calcite peak compared with the control after 24 h. Notably, the activation effect was prominent in C 0.5, although the initial Ca^{2+} dissolution was highest in C 1.0. This indicated that an excessive amount of $Ca(NO_3)_2$ was detrimental to the activation of LLC carbonation in terms of precipitation. This can be attributed to the abrupt formation of a reaction-product layer on the LLC, which hinders the diffusion of CO_2 into the sample.

The samples activated by $Mg(NO_3)_2$ exhibited distinct alterations in peak evolution. The most significant differences were observed in the widths and positions of the peaks near 2θ= 29°–30°. As shown in Fig. 8 (d)–(f), the main peaks of calcite presented broader shapes owing to the evolution of a shoulder peak near 2θ= 29.7°. This is attributed to the generation of Mg-calcite ($Ca_{(1-x)}Mg_xCO_3$) owing to the incorporation of Mg atoms into the calcite structure [43,53]. This contributes to the formation of a solid solution consisting of Mg-calcite and calcite. After 3 h of CO_2-curing, the formation of Mg-calcite was observed only at M 0.5, which indicates a rapid reaction compared with that at the other concentrations. Similar to $Ca(NO_3)_2$, the samples activated by all concentrations of $Mg(NO_3)_2$ showed distinct changes in the peak evolution of calcite and Mg-calcite after 6 h, and this modification of carbonate formation was most prominent in the samples treated with 0.5 M.

The carbonate content in the LLCs activated by $Ca(NO_3)_2$ and $Mg(NO_3)_2$ was quantified, as depicted in Fig. 9. For both nitrates, the concentration of 0.5 M showed the most significant enhancement in carbonate formation. As shown in Fig. 9(a), the samples treated with $Ca(NO_3)_2$ showed higher amounts of calcite, rather than vaterite and aragonite, compared with the control sample. Notably, the amounts of vaterite and aragonite were similar between the control and C 0.5 although the total $CaCO_3$ content in C 0.5 was almost 1.8 times higher. This indicates that the addition of Ca^{2+} through direct dissociation from $Ca(NO_3)_2$ and enhanced dissolution from the LLCs contributed to the crystallization of carbonates into calcite, which is the most stable polymorphism of $CaCO_3$. C 0.1 formed a smaller amount of carbonates than Control until 6 h, consistent with its lower early DoR. C 1.0 generated a smaller amount of carbonates owing to the supersaturation of Ca^{2+} interrupting the transport and dissolution of CO_2 owing to the excessively increased ionic strength, thereby terminating the surface reaction. The early and sustained carbonate formation in C 0.5 corresponded to its rapid strength development from 3 h onward.

The samples activated by $Mg(NO_3)_2$ in Fig. 9(b) exhibited trends different from those activated by $Ca(NO_3)_2$. In contrast to the C group, which formed abundant calcite, the M group formed Mg-calcite with the addition of $Mg(NO_3)_2$, causing the amount of calcite to be lower than that of the C group. The total carbonates and Mg-calcite increased drastically along with the addition of $Mg(NO_3)_2$ until 0.5 M and decreased again at 1.0 M. Improved initial Ca^{2+} dissolution activated the reaction and precipitation of carbonates in the M group, whereas the excessive amount of $Mg(NO_3)_2$ yielded the rapid formation of $CaCO_3$ on the surface, hindering further reaction. The amounts of vaterite and aragonite in the M group were lower than those in the control group, except for M 1.0. It is plausible that the large amount of Mg in M 1.0 is involved in the crystallization of carbonates, stabilizing vaterite and aragonite, which are known to be metastable. However, the vaterite and aragonite in M 1.0 reconverged into calcite and Mg-calcite with the progress of CO_2-curing.

The total amount of carbonate in C 0.5 after 24 h was significantly higher than that in M 0.5. At 0.5 M, Ca^{2+} was more effective in the

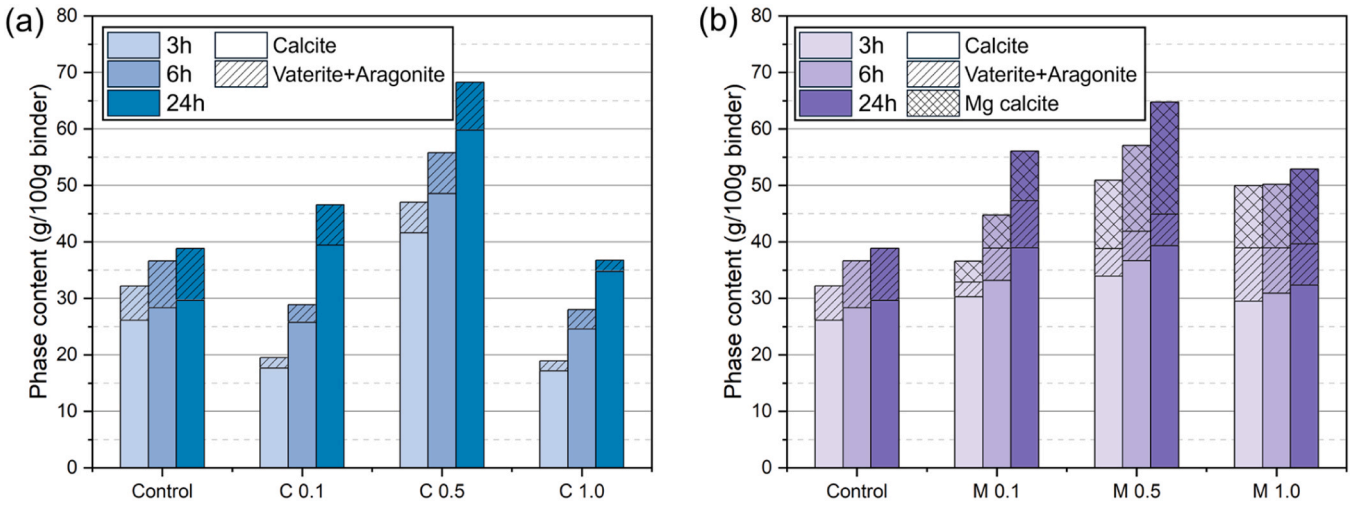

Fig. 9. Carbonate contents in the CO_2-cured LLCs activated by (a) $Ca(NO_3)_2$ and (b) $Mg(NO_3)_2$.

formation of carbonates, as it consisted of identical cations constituting $CaCO_3$. Conversely, the incorporation of Mg^{2+} shifted the equilibrium of crystal stabilization, possibly hindering the stabilization of the calcite crystals.

The changes in the major diffraction peaks of the reactant phases (CS and C_2S) under different concentrations of $Ca(NO_3)_2$ and $Mg(NO_3)_2$ according to CO_2-curing are compared in Fig. 10. Among the samples activated by $Ca(NO_3)_2$ (Fig. 10 (a)–(c)), C 0.5 displayed the most distinct and rapid initial reaction of C_2S and CS. Both reactants were consumed rapidly in C 0.5, and CS was further consumed after the depletion of C_2S. This sequential consumption is attributed to the higher reactivity of C_2S than CS [98]. C 1.0 showed a slow initial consumption of C_2S at 3 h; however, these phases decreased steadily until 6 h and 24 h, finally reaching the near-extinction of the C_2S peaks. In contrast, C 0.1 showed a slow consumption of C_2S from the early stage (3 h), leaving residual peaks of the reactants even at 24 h.

Compared with $Ca(NO_3)_2$, $Mg(NO_3)_2$ also induced a notable decrease in the diffraction peaks of C_2S in M 0.5, nearly all of which were consumed during the initial stage (3 h). After consuming C_2S, CS reacted steadily until 24 h, contributing to further reaction progress. M 1.0 also showed a significant decrease in the diffraction peaks of reactant phases and exhibited steady consumption throughout CO_2-curing, accelerating from 6 h and finally reaching the extinction of the C_2S peaks at 24 h. M 0.1 showed a slow but steady decrement of the diffraction peaks of C_2S as well, in contrast to C 0.1, which exhibited the lowest consumption of the reactant phases.

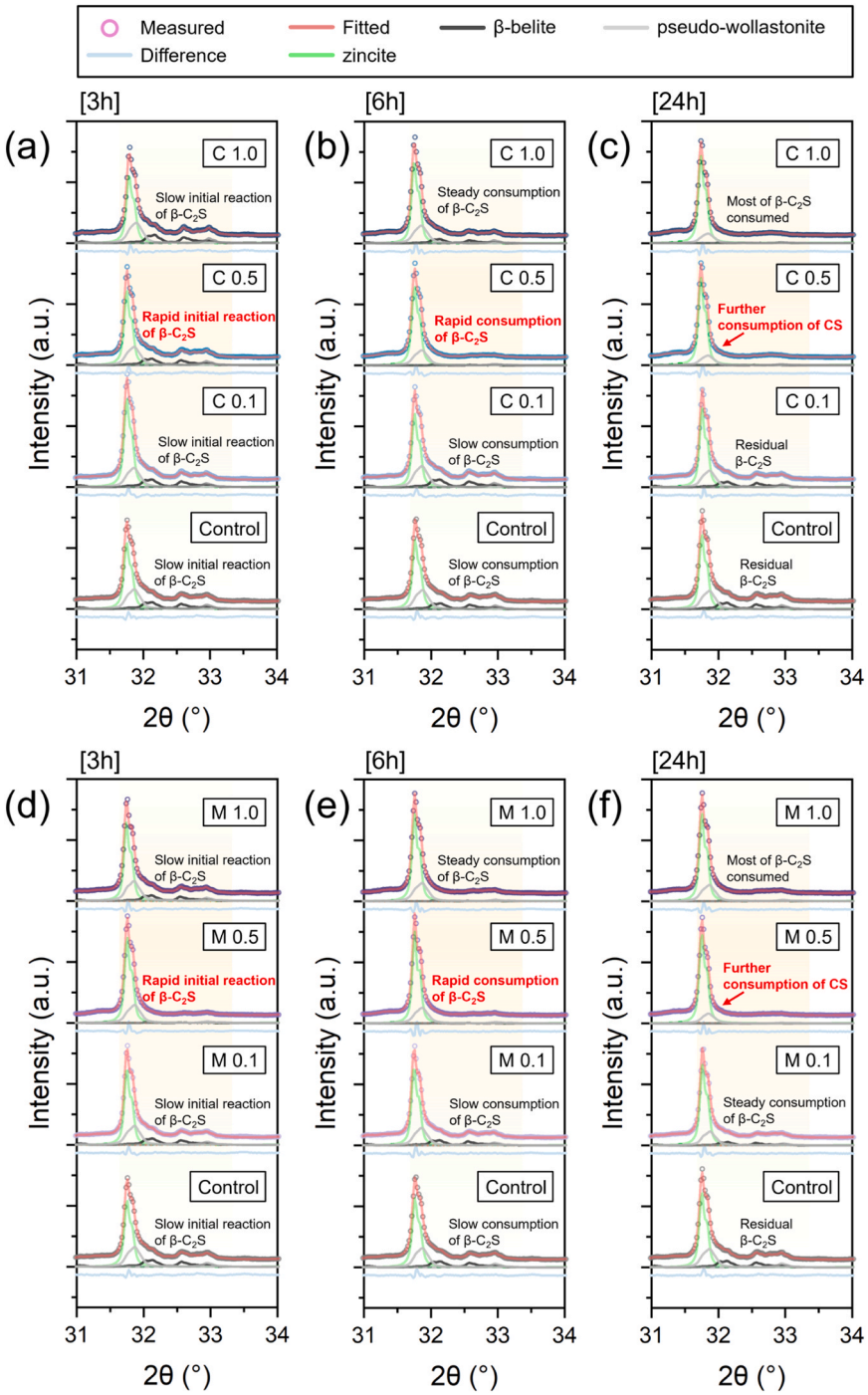

Fig. 10. Refined XRD patterns of the CO_2-cured LLCs activated by (a)–(c) $Ca(NO_3)_2$, and (d)–(f) $Mg(NO_3)_2$ at $2\theta = 31°–34°$.

The consumption of the reactant phases in the LLC pastes upon activation was evaluated quantitatively, as shown in Fig. 11. Both samples treated with $Ca(NO_3)_2$ (Fig. 11 (a)) and $Mg(NO_3)_2$ (Fig. 11 (c)) exhibited the highest DoR from the early stage (after 3 h) at a molar concentration of 0.5 M.

In the LLCs activated by $Ca(NO_3)_2$ (Fig. 11 (a)), the samples activated by the concentration of 0.5 M showed substantial reactivity enhancement from the early stage in contrast to the concentrations of 0.1 M and 1.0 M. Limited (0.1 M) or excessive (1.0 M) amounts of $Ca(NO_3)_2$ exhibited even lower DoR than the samples without activation for 6 h. This reduction in the DoR at 0.1 M and 1.0 M at an early stage can be explained by different phenomena.

At 0.1 M, C 0.1 exhibited a transient reduction in DoR relative to Control during the first 6 h, indicating that this concentration of $Ca(NO_3)_2$ did not effectively promote the early reaction. Dissolved Ca^{2+} might adsorb onto the particle surface and interfere with the surface charge layer [131,132], forming a layer suppressing further dissolution and delaying the initiation of carbonation. Conversely, at 1.0 M, the solution became highly enriched with Ca^{2+}, leading to the rapid attainment of near-supersaturation conditions upon CO_2 dissolution. This promoted preferential and abrupt $CaCO_3$ precipitation, reducing the coupling of dissolution and carbonation necessary for efficient reaction propagation. The excessive ionic strength of 1.0 M also hindered CO_2 transport toward the surface, collectively delaying effective carbonation and resulting in a reduced early-age DoR. Nevertheless, C 0.1 and C 1.0 consequently exceeded the DoR of the control at 24 h owing to the resultant activation effect.

Notably, C 0.5 yielded an exceptionally high DoR (two times higher than that of the control) from an early stage by compromising neither surface accessibility nor dissolution kinetics; instead, it provided the

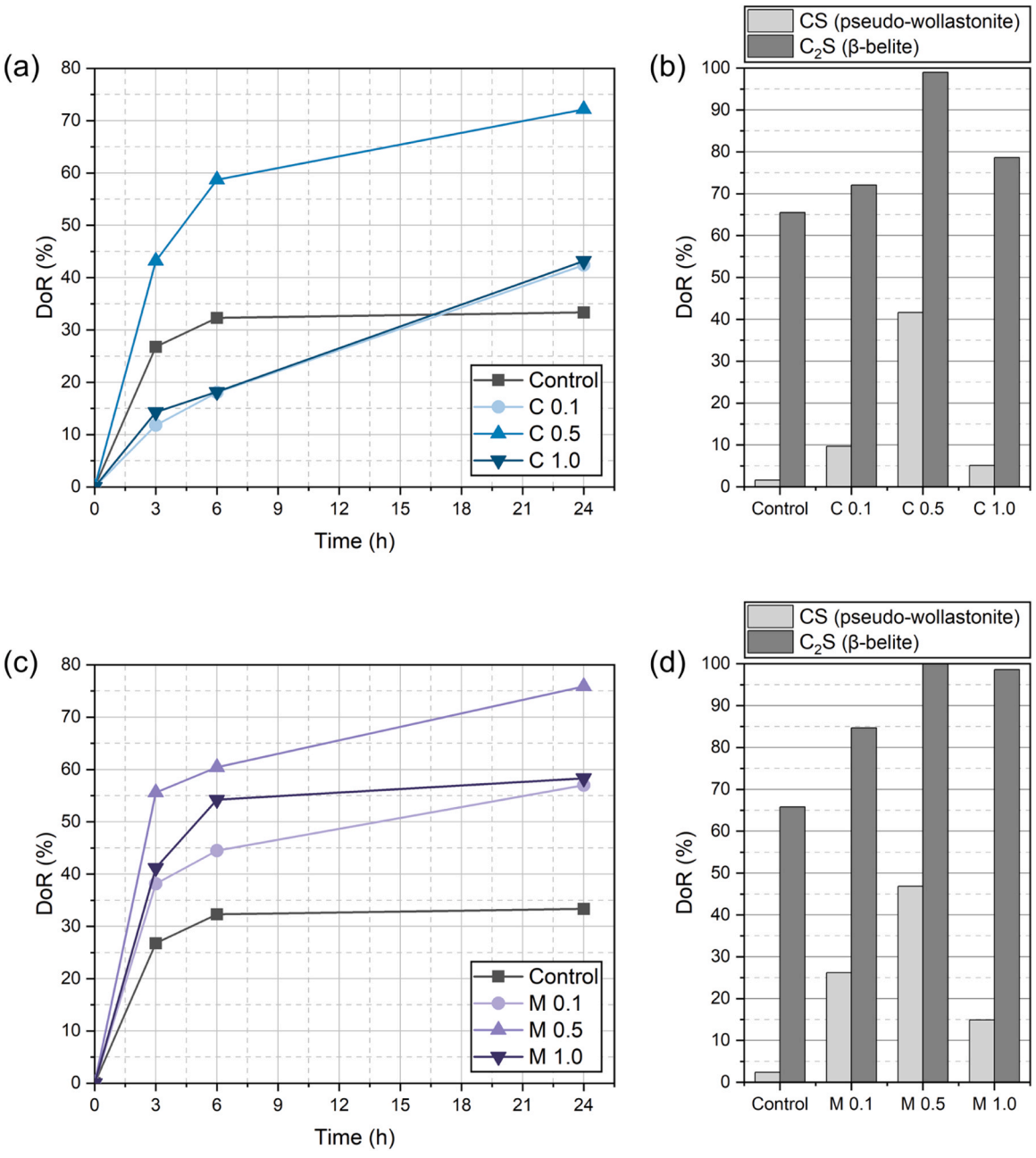

Fig. 11. DoRs of the CO_2-cured LLCs activated by $Ca(NO_3)_2$ ((a) and (b)) and $Mg(NO_3)_2$ ((c) and (d)).

favorable ionic environment that maximized both dissolution and carbonation. In contrast, the LLCs activated by $Mg(NO_3)_2$ (Figs. 5–8(c)) showed enhanced reactivity from the early stage (after 3 h) at all concentrations (0.1, 0.5, and 1.0 M). Similar to the trend observed with $Ca(NO_3)_2$, the highest DoR was achieved at 0.5 M; however, both 0.1 M and 1.0 M also exhibited substantial improvements in reactivity.

$Mg(NO_3)_2$ exerts effects distinct from those of $Ca(NO_3)_2$ during carbonation. The contrasting behaviors of C 0.1 and M 0.1 indicate that the early reaction response depended not only on the nitrate concentration but also on the cation species. The distinct characteristics of Ca^{2+} and Mg^{2+} may have contributed to their different influences on the interfacial reaction and carbonate precipitation [133,134]. However, because the relevant surface interactions were not directly characterized, their specific contributions could not be resolved in this study.

The DoRs of C_2S and CS after 24 h of CO_2-curing, which are the main reactant phases of the LLCs, are evaluated in Fig. 11 (b) and (d). The $Ca(NO_3)_2$-activated samples in Fig. 11 (b) showed a prominent increase in the DoR of C_2S, reaching 98% in C 0.5. The increase in the DoR of CS was also remarkable (42% in C 0.5), considering that the DoR of CS in the control group was only 3%. The samples activated by $Mg(NO_3)_2$ presented higher DoRs for both C_2S and CS than those activated by $Ca(NO_3)_2$ owing to the beneficial action of Mg^{2+}. These results indicate that adequate concentrations of both $Ca(NO_3)_2$ and $Mg(NO_3)_2$ can substantially improve reactivity, contributing to the effective use of LLCs. The differences in residual water content after pre-curing may also have partly influenced the carbonation reaction. However, considering the relatively small differences compared to the variables in related research [81], the effects of water content were considered secondary to the activation effects of nitrates dependent on the concentrations.

It should be noted that the high absolute DoR values obtained in this study were also influenced by the small specimen dimensions same as in the compressive strength. The maximum CO_2 diffusion distance in the specimens was approximately 2.5 mm, which likely facilitated extensive carbonation throughout the specimens within 24 h. Therefore, the DoR results should also primarily be interpreted through relative comparisons among the control and nitrate-activated samples tested under identical specimen geometries and curing conditions. The influence of specimen size on the applicability of these results to larger components is further discussed in Section 3.6.

The phase evolutions of the LLCs activated by $Ca(NO_3)_2$ and $Mg(NO_3)_2$, considering the weight gain during the reaction, are shown in Fig. 12. In the control (Fig. 12 (a)), the reactant phases (C_2S, C_3S_2, and CS) were rapidly consumed up to 6 h, followed by a gradual decrease until 24 h. Reaction products ($CaCO_3$ and amorphous phases from the Ca-modified silica gel) were generated owing to the carbonation of the reactants. The amount of crystalline SiO_2 phases remained relatively constant because they are inert to carbonation at ambient temperature and pressure [135,136].

The activated samples (Fig. 12 (b)–(g)) displayed significant increases in the total phase content compared with the control (Fig. 12 (a)) because of the higher amounts of $CaCO_3$ induced by the greater consumption of the reactant phases. Notably, the activated samples exhibited continuously decreasing reactants and increasing products throughout CO_2-curing, which were distinguished from the phase evolution of the control, showing convergence after 3 h.

The samples activated by $Ca(NO_3)_2$ presented calcite as the main reaction product, with a substantial increase in the amount at a specific concentration (0.5 M). In contrast, the $Mg(NO_3)_2$-activated samples possessed Mg-containing carbonates as the main product, as well as $CaCO_3$ crystals, as shown in Fig. 8. Mg in carbonate is preferred in Mg-calcite, considering that the environment is unfavorable for the formation of other Mg-containing carbonates (magnesite, dolomite, and hydromagnesite) [137,138]. The amount of Mg incorporated into the sample was too low to produce magnesium carbonate phases, contributing to the crystallographic alteration of calcite by substituting the Ca^{2+} sites.

The TGA of the CO_2-cured LLCs revealed CO_2 fixation characteristics, including the formation of ACC and improved fixation capability through activation. The derivative thermogravimetric (DTG) curves of the LLC pastes are shown in Fig. 13 (a)–(d). All the activated samples displayed DTG peaks according to weight loss in the range 300–830 ℃, which is known to be the conventional decomposition of $CaCO_3$ in carbonated LLCs [27,34,43,139]. In the $Ca(NO_3)_2$-activated samples (C group in Fig. 13 (a) and (b)), the evolution of the DTG peak at 600–830 ℃ attributed to the crystalline $CaCO_3$ was distinct throughout the increase in CO_2-curing time [27,140,141]. The DTG peak was the highest in C 0.5 at both 3 h and 24 h. C 0.1 and C 1.0 displayed a DTG peak lower than that of the control at 3 h, which was compensated at 24 h through the activation effect shown in the XRD results (Fig. 9). Note that the rise in the DTG peak at 600–830 ℃ with the addition of $Ca(NO_3)_2$ was significant, indicating that the Ca^{2+} supply through $Ca(NO_3)_2$ facilitated the crystallization of $CaCO_3$ during the reaction. The DTG humps of the $Ca(NO_3)_2$-activated samples at 300–600 ℃ also showed a different shape from the control, indicating the earlier decomposition of ACC.

The $Mg(NO_3)_2$-activated samples showed similar trends to those of $Ca(NO_3)_2$, aligning well with the XRD results (Fig. 9). However, the samples activated by $Mg(NO_3)_2$ exhibited an apparently higher evolution of hump in the temperature range of 300–600 ℃, attributed to the ACC from 3 h (Fig. 13 (c) and (d). Considering the formation of Mg-calcite evidenced in the XRD results, the presence of Mg^{2+} prohibited the crystallization of $CaCO_3$ during precipitation, leading to the formation of a higher amount of ACC and the consequent formation of Mg-calcite. The improvement in CO_2 fixation according to activation is shown in Fig. 13 (e) and (f). Both $Ca((NO_3)_2$ and $Mg(NO_3)_2$ exhibited outstanding CO_2 sequestration capability at 0.5 M, presenting a 1.5–1.6 times higher value than that in the samples without activation. The amount of CO_2 fixed at other concentrations followed the trend of the XRD results, aligning well with the DoR. A comparison of the carbonates determined using QXRD and TGA is shown in Fig. 14. The samples activated with $Ca(NO_3)_2$ generally followed the $y = x$ curve, indicating that the $Ca(NO_3)_2$ addition facilitated the crystallization of $CaCO_3$ during precipitation. In contrast, the carbonate contents determined by QXRD in the samples activated with $Mg(NO_3)_2$ were generally underestimated compared with those determined by TGA, proving that the chemical environment driven by $Mg(NO_3)_2$ was favorable for the formation of ACC, which can hardly be detected by XRD.

As shown in Fig. 15, the silicate chain structure in the amorphous Ca-modified silica gel phase, which is another important reaction product during the carbonation of LLCs, was investigated. Unreacted LLC exhibited numerous resonances in the chemical shift range of −68 to −76 ppm, corresponding to orthosilicate (Q^0). The peaks centered at −79.6 ppm and −85.3 ppm are attributed to Q^1 (chain-end) and Q^2 (middle-chain) tetrahedra, which included in the C_3S_2 (sorosilicate structure) and CS (cyclic silicate ring structure of $Si_3O_9^{6-}$) respectively, therefore their content can be explained through the residual reactant phases. [26,94,142]. All the LLC samples showed significant resonances in the Q^3 (crosslinked-chain) and Q^4 (fully polymerized-chain) regions, consistent with the formation of highly polymerized silicate chains in the Ca-modified C–S–H and silica gel in the presence of CO_2 [143,144]. The control sample showed notable Q^0 remnants, indicating unreacted LLCs. The proportions of Q^1 and Q^2 were also higher than those in C 0.5 and M 0.5, which indicates that the amount of residual unreacted phase was higher. In contrast, C 0.5 and M 0.5 presented significantly larger area fractions of Q^4 with scant Q^0, indicating a higher degree of silicate polymerization owing to enhanced carbonation reactivity. C 0.5 exhibited an even larger Q^4 area fraction and less contribution from Q^1, Q^2, and Q^3 compared with M 0.5, which agrees well with the superior DoR improvement effect of $Ca(NO_3)_2$ at a later stage, as evidenced by the QXRD results (Fig. 11). M 0.5 presented a characteristic Q^2 peak despite its high DoR, which has been reported to be a trace of modified magnesium silicate hydrate (M–S–H) gel, which may have been generated by the supply of Mg during the silicate polymerization process [43,145,146].

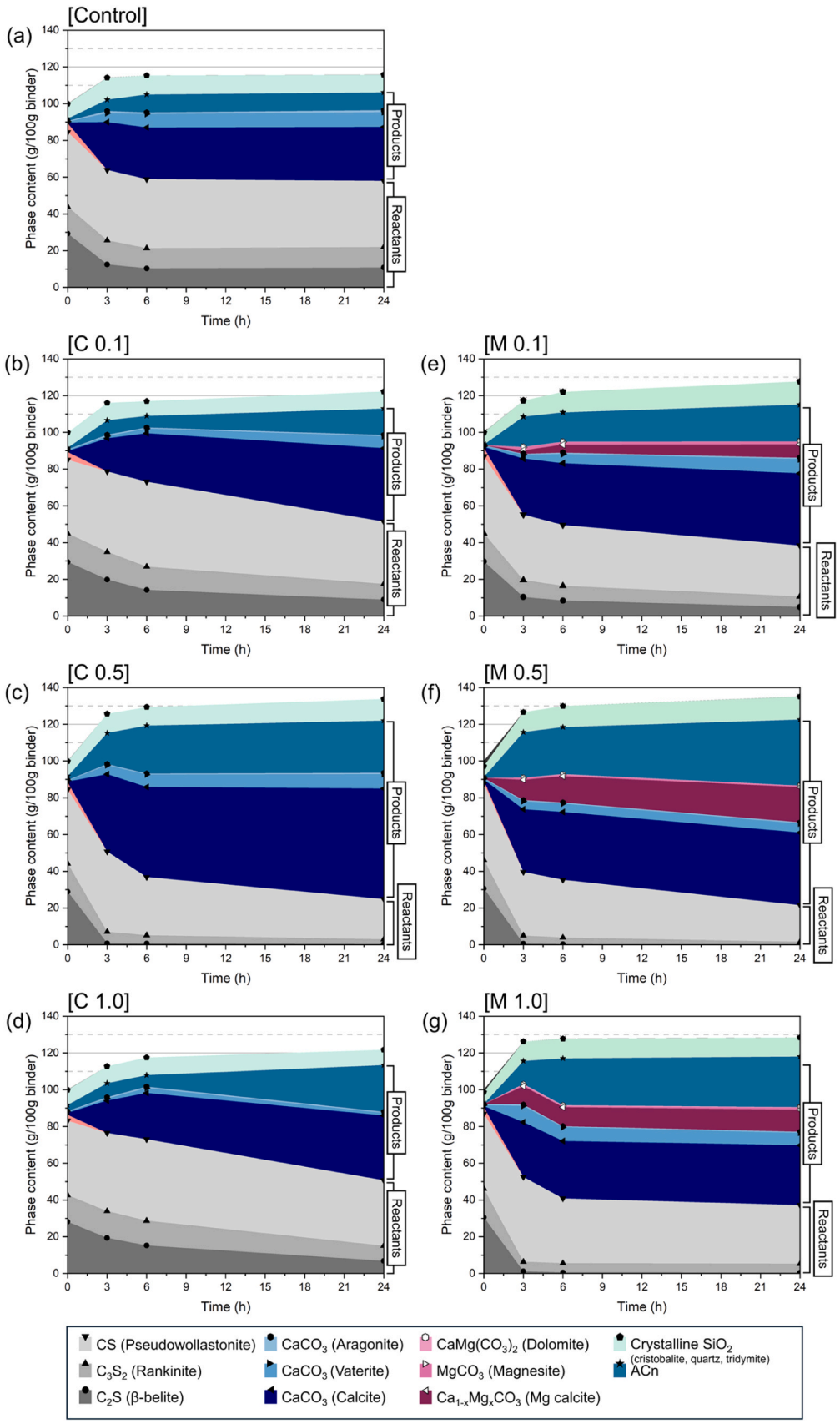

Fig. 12. Phase evolution of the CO_2-cured LLCs activated by (b)–(d) $Ca(NO_3)_2$ and (e)–(g) $Mg(NO_3)_2$.

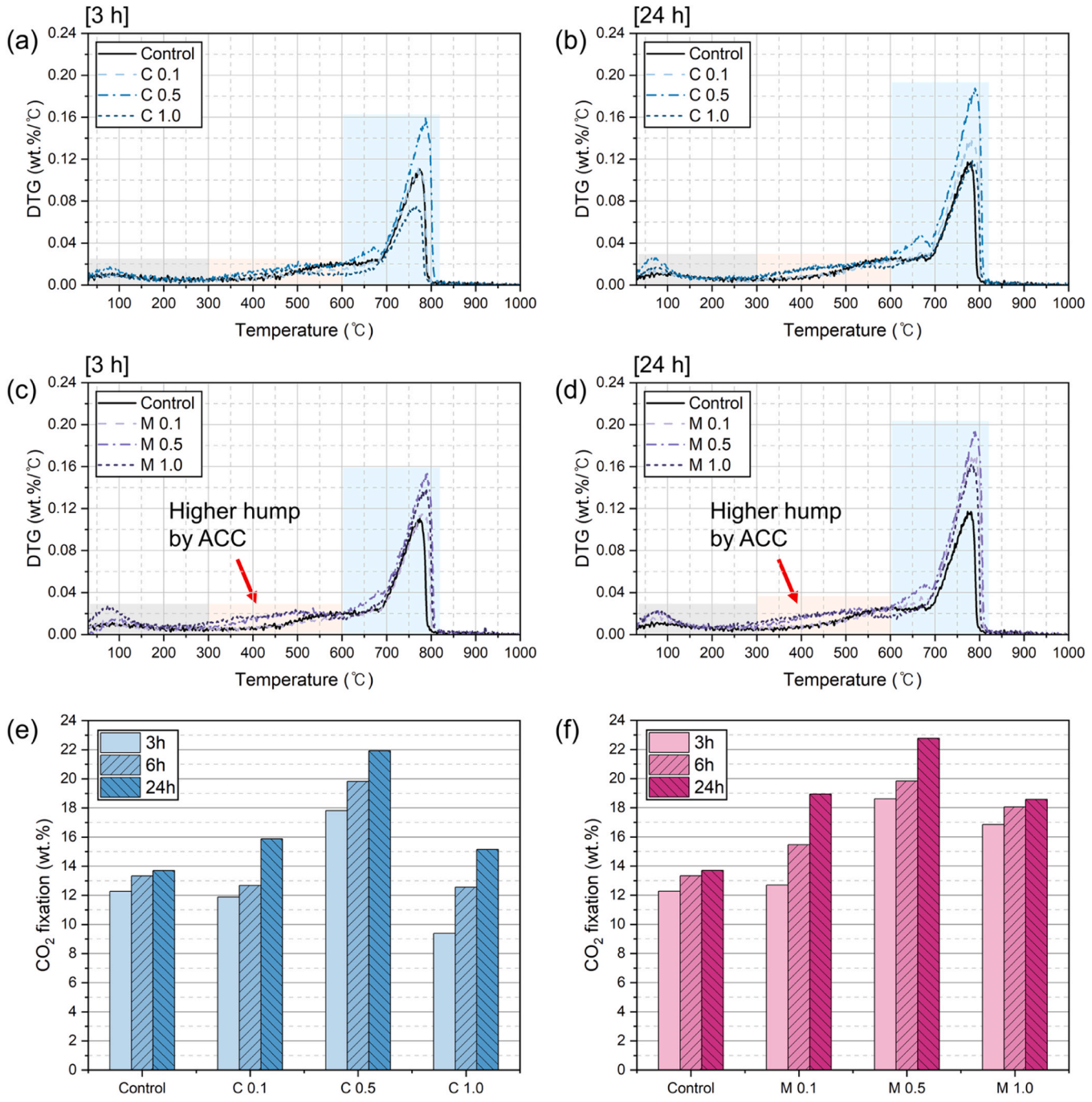

Fig. 13. TGA of the CO_2-cured LLC pastes activated by $Ca(NO_3)_2$ and $Mg(NO_3)_2$. (a)–(d) derivative TG curves and (e)–(f) CO_2 fixation.

At 0.5 M, both nitrate induced extensive consumption of reactant and carbonate formation in LLCs, consistent with their substantial strength gains relative to Control. However, the comparison between C 0.5 and M 0.5 shows that reaction extent alone did not determine the mechanical performance. M 0.5 exhibited higher DoRs of the major calcium silicate phases, whereas C 0.5 produced a slightly larger amount of crystalline carbonate and achieved the higher compressive strength. The distribution of reaction products including calcite, ACC, and Mg-calcite was therefore important in interpreting how the phase formation affected the mechanical performance. The corresponding features are examined in Sections 3.4 and 3.5.

3.4. Reaction kinetics of activated LLCs

To further investigate the phase formation mechanisms of LLCs under the concentrations which provided the highest performance among the examined conditions, the phase evolutions of the single particles of the control, C 0.5, and M 0.5 were analyzed. The reaction of each sample can be divided into three stages in which an abrupt change in the phase evolution occurs. As previously discussed in the QXRD results (Fig. 12), C 0.5 and M 0.5 (Fig. 16 (b) and (c)) underwent significant activation in the reaction after the initial stage compared with the control (Fig. 16 (a)), where the reaction gradually converged after a

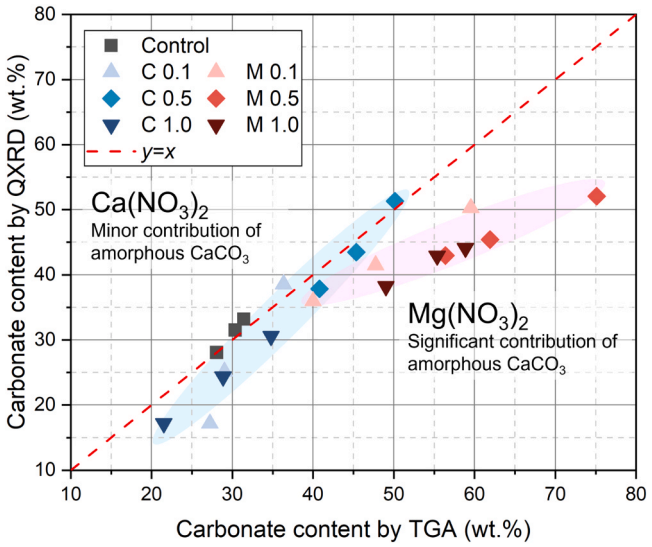

Fig. 14. Comparison of the total $CaCO_3$ content determined using TGA and XRD.

specific time. Notable amounts of calcite and Mg-calcite were observed in C 0.5 and M 0.5, respectively, starting from Stage II.

Fig. 16 (d)–(f) show the reaction kinetics model fitting results for the LLC samples with and without activation. Parameter *k* is a reaction constant that represents the apparent value of the rate constant, as the intrinsic reaction rate constant requires the explicit consideration of additional experimental variables. The control sample showed a gradual decrease in *k* from Stage I to Stage III owing to the transition of the reaction mode from a phase boundary reaction to a diffusion-driven reaction [66,147,148]. Stage II in the control can be regarded as a transient stage in which the reaction mode converts from a phase boundary to a complete diffusion-based condition [100]. In contrast, C 0.5 and M 0.5 exhibited a significant increase in the rate constant in Stage II, and *k* decreased again in Stage III. This demonstrates that the reaction was activated in Stage II, according to the incorporation of nitrates. Note that the activation in M 0.5 started earlier than that in C 0.5, possibly because of the electrolyte layer, as discussed previously. The reaction constants (*k*) at the respective reaction stages are summarized in Table 5. The reaction constant k_1 at Stage I was higher than those of C 0.5 and M 0.5, indicating that the reaction was faster without nitrates at a very early stage (within 60 min). However, this fast reaction at an early stage results in the formation of a reaction product barrier layer, hindering further reaction and rapidly converting the rate-controlling stage to diffusion [97,149,150]. In contrast, the lower initial reaction constants k_1 in C 0.5 and M 0.5 suggest that nitrate addition initially suppressed the early stage reaction owing to the interaction between the LLCs and diverse ions in the environment controlled by $Ca(NO_3)_2$ and $Mg(NO_3)_2$. This behavior can be interpreted as an induction period extension, during which the premature formation of the reaction product barrier is delayed and the time for the sufficient dissolution of LLC is yielded. Consequently, C 0.5 and M 0.5 underwent an activated reaction in Stage II, with an increased constant (k_2). After the activation stage was completed and the reaction was converted to the diffusion-driven stage, C 0.5 and M 0.5 still showed a much higher reaction constant (k_3) than the control, owing to the high concentration of dissolved ions from the previous stages. This temporal control of reaction rate is relevant to the mechanical properties observed in Fig. 5. Rather than exhausting the reaction during the initial period, C 0.5 and M 0.5 maintained product formation during the later stages, enabling continued densification of the matrix and the substantial strength gains. The potential implication of this extended induction behavior for CO_2 transport and carbonation in larger specimens is further discussed in Section 3.6.

The morphological characteristics of the reaction products in the single particle samples of the control, C 0.5, and M 0.5 are shown in Fig. 17. In the control samples in Fig. 17 (a), the $CaCO_3$ nuclei generated on the surface at a very early stage grew continuously to form $CaCO_3$ crystals with coarse mechanical interlocks. Alterations in the formation mechanisms during growth were barely observed, corresponding to a continuous decrease in the reaction constant k (Fig. 16). In contrast, C 0.5 and M 0.5 exhibited the characteristic morphological evolutions of their respective reaction products. In C 0.5 (Fig. 17 (b)), a higher number of nanosized nuclei were formed on the surface of the particle owing to the increased initial Ca^{2+} concentration activated by $Ca(NO_3)_2$. The crystals grew rapidly from the nuclei to form microstructures consisting of both bulk and nanosized crystals. These nanosized crystals adsorbed onto the bulk crystals were consumed after specific CO_2-curing (from the diffusion-driven stage), thereby feeding the bulk crystals to grow further. This phenomenon can be explained by Ostwald ripening [151,152], as shown in Fig. 18 (b). The LLCs samples activated by Ca $(NO_3)_2$ dissociated higher amounts of Ca^{2+}, creating an environment

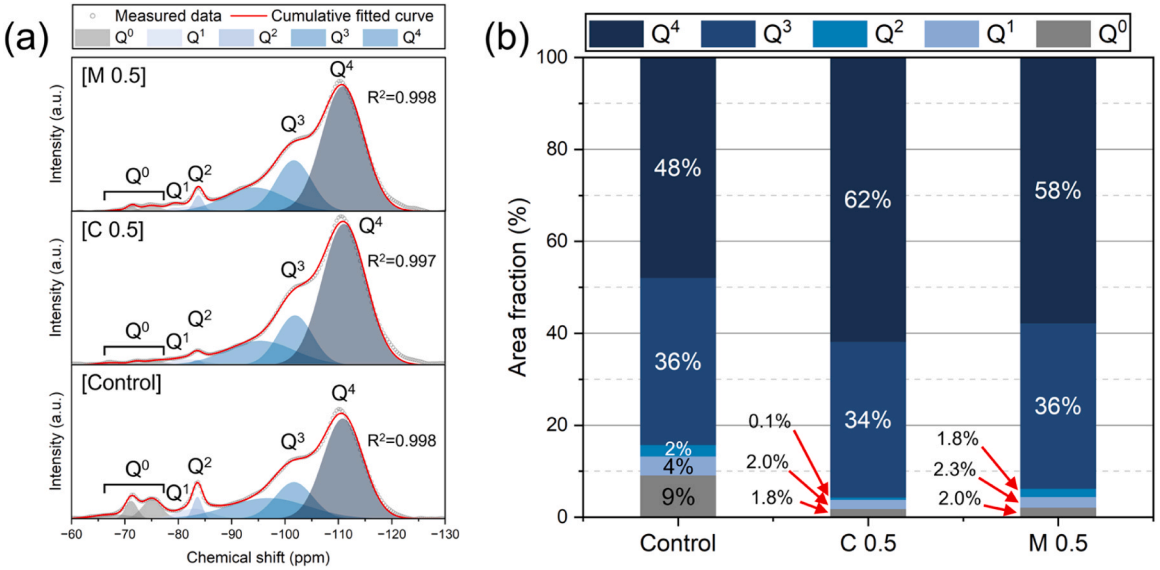

Fig. 15. Silicate chain structure analysis using ^{29}Si NMR: (a) deconvoluted spectra and (b) area fraction of Q^n species.

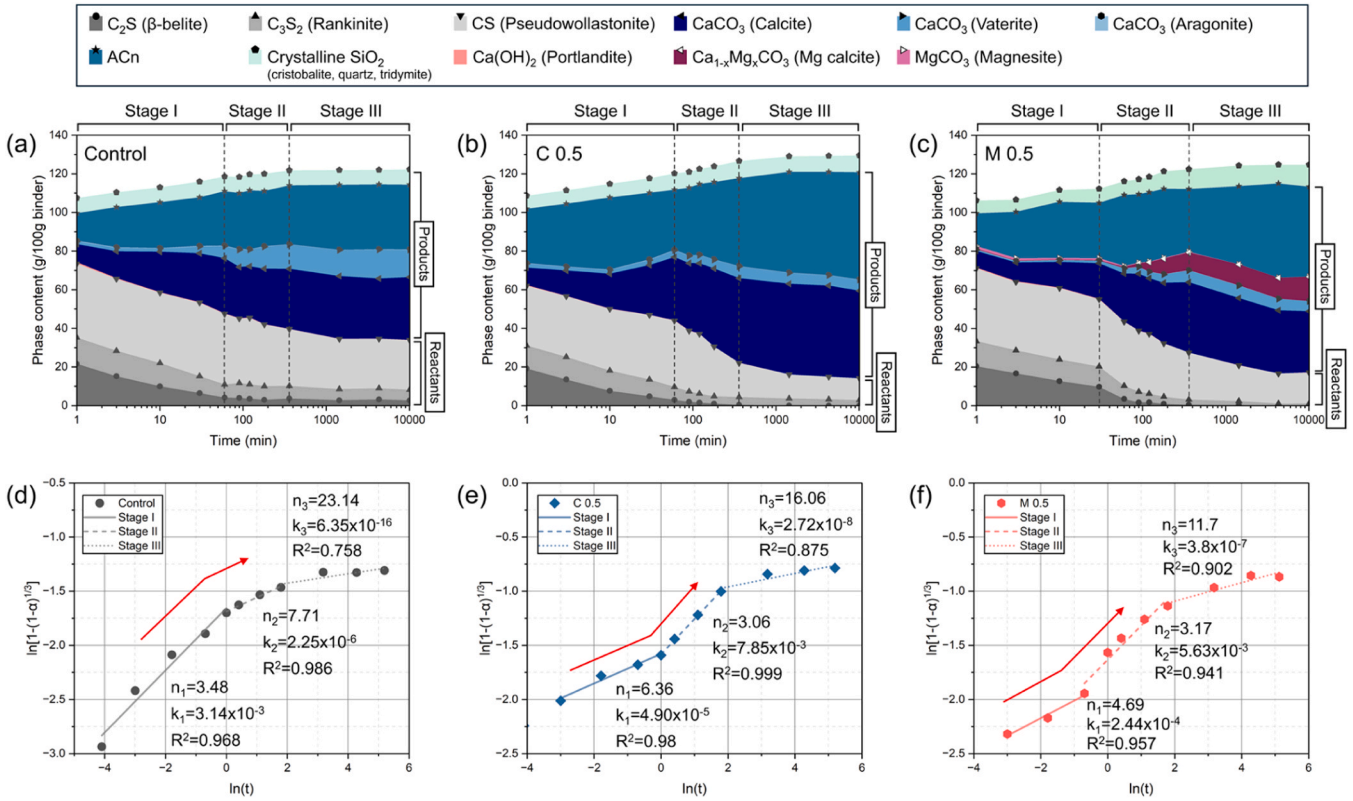

Fig. 16. Reaction kinetics of LLCs with/without activation during CO_2-curing (a)–(c) phase assemblage and (d)–(f) DoR fitted by theoretical solid-gas kinetic models.

Table 5
Comparison of the rate constant of the LLCs with/without activation.

Reaction stage	Rate constant *k*		
	Control	C 0.5	M 0.5
I	3.14×10^{-3}	4.90×10^{-5}	2.44×10^{-4}
II	2.25×10^{-6}	7.85×10^{-3}	5.63×10^{-3}
III	6.35×10^{-16}	2.72×10^{-8}	3.80×10^{-7}

favorable for the formation of nanocrystalline $CaCO_3$ [153]. This nanocrystalline $CaCO_3$ was generated along with the bulk $CaCO_3$ until Stage II and was subsequently consumed to form larger $CaCO_3$ crystals in Stage III.

As shown in Fig. 17 (c), the formation mechanisms of M 0.5 differed from those of C 0.5. The initial supply of Ca^{2+} from the LLCs was activated similarly, the nuclei grew rapidly on the surface, and the presence of Mg^{2+} influenced the formation kinetics of $CaCO_3$. Mg^{2+} hinders crystallization, resulting in the formation of amorphous $CaCO_3$ [154, 155]. After a certain period, Mg-calcite with rounded and polyhedral shapes was formed, rather than rhombic morphologies. As shown in Fig. 18 (c), these similarly sized crystals grew further and aggregated. The aggregated solids merged and became coalescent [156–158]. These coalescent Mg-calcites formed an enhanced interlocked microstructure characterized by smaller crystal sizes than those in C 0.5.

These contrasting growth of calcium carbonates provide a further explanation for the differences in mechanical properties between the activated samples. In C 0.5, Ostwald ripening generated larger calcite crystals with extensive inter-crystalline contact, whereas M 0.5 developed an assembly of smaller polyhedral Mg-calcite particles through aggregation and coalescence. Both product structures supported high strength, but the more extensively intergrown calcite domains in C 0.5 likely contributed to higher compressive strength.

3.5. *Pore structure refinement of LLCs activated by $Ca(NO_3)_2$ and $Mg(NO_3)_2$*

The microstructural refinement of the LLCs activated by $Ca(NO_3)_2$ and $Mg(NO_3)_2$, as observed via SEM-BSE, is shown in Fig. 19. The activated samples exhibited a densified microstructure compared with the control, but the distribution and size of the pores differed. In the control sample (Fig. 19 (a) and (d)), relatively large pore areas were observed, which were irregularly shaped and widely distributed throughout the matrix. These pores appeared as isolated voids and locally connected regions, indicating the incomplete filling of the pore space by the reaction products. The matrix surrounding the pores was heterogeneous, with distinct boundaries between the unreacted particles and the carbonation products, suggesting limited reaction progress. In contrast, C 0.5 (Fig. 19 (b) and (e)) exhibited a noticeable reduction in the overall pore fraction. The dark regions were smaller and more uniformly dispersed, and large interconnected pores were rarely observed. The matrix appeared more continuous, with the pores partially or fully surrounded by the reaction products. This microstructural refinement is consistent with the increased formation of $CaCO_3$ identified by phase quantification, indicating that enhanced Ca^{2+} availability promotes the precipitation of carbonation products within the microstructure. M 0.5 (Fig. 19 (c) and (f)) showed the most pronounced reduction in visible pore area. The pores were finer and more homogeneously distributed than those in the $Ca(NO_3)_2$-activated samples. A dense and uniform matrix was formed, with pores predominantly appearing as isolated small voids rather than as clustered features. M 0.5 generally showed decreased pore sizes; however, some of the regions in C 0.5 were denser than those in M 0.5.

The difference between the microstructures of the LLCs activated by $Ca(NO_3)_2$ and $Mg(NO_3)_2$ is attributed to the characteristic crystal formation mechanisms shown in Fig. 18. Activation by $Ca(NO_3)_2$ induces the growth of enlarged rhombohedral crystals, whereas activation by $Mg(NO_3)_2$ leads to the formation of smaller rounded crystals. Both

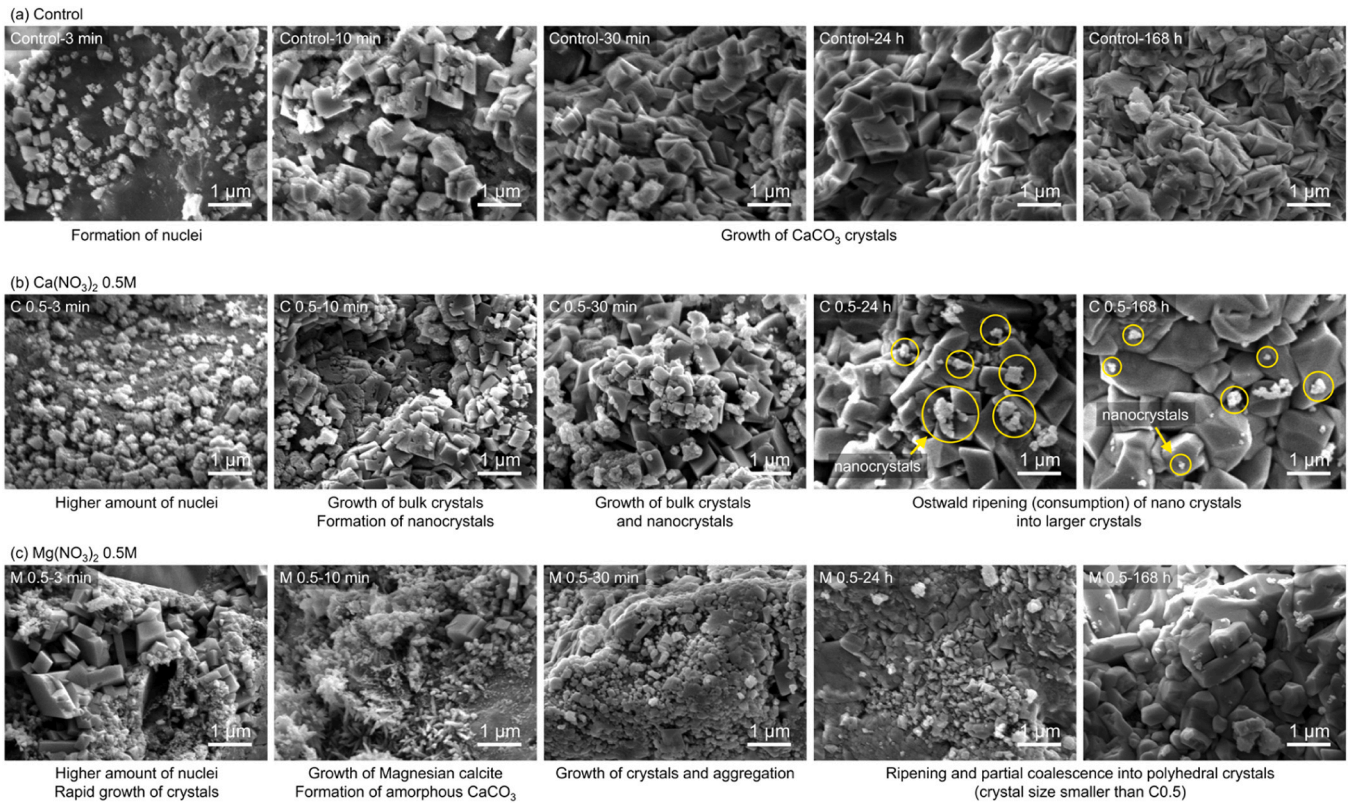

Fig. 17. Morphological observations for the reaction products of the LLCs during CO_2-curing (a) without activation, (b) C 0.5, and (c) M 0.5.

effectively densify the microstructure; however, compaction by larger crystals causes the inhomogeneous generation of larger pores with agglomeration, leading to a heterogeneous microstructure. Conversely, the formation of smaller crystals in M 0.5 led to a highly homogeneous and refined microstructure with a significantly decreased pore volume.

The pore characteristics in the LLC pastes were statistically investigated using X-CT. The reconstructed 2D slice images and 3D volumes of the LLCs are shown in Fig. A3. Pore volume analysis revealed that the activation by $Ca(NO_3)_2$ induced a pore structure with the least porosity and high heterogeneity, characterized by the distribution of pores with larger sizes. In contrast, $Mg(NO_3)_2$ resulted in the smallest individual pore sizes with moderate densification and high homogeneity.

The pore volumes of the CO_2-cured LLCs with different activation methods are compared in

Fig. 20. C 0.5 and M 0.5 showed a significant reduction in pore volume, which was less than half that of the control. The decrease in the number of pores with diameters between 1000 and 2000 nm was remarkable, and densification occurred through the growth of $CaCO_3$ crystals (Fig. 19). In M 0.5, pores with the diameters of 3000–4000 nm nearly diminished, which is consistent with the SEM observations (Fig. 19). Notably, C 0.5 exhibited the lowest total pore volume, whereas the quantity of smaller individual pores were higher in M 0.5. Respective samples therefore achieved pore refinement through different synergistic effects of pore volume and pore size, which may partly account for their distinct mechanical properties. The cumulative volume distribution in Fig. 20 (b) also demonstrates that the size of the individual pores was smaller in M 0.5. Fig. 20 (c) shows the distribution of the regional porosities in the respective samples. In the control group, the mean porosity was 12.2%, whereas the regional porosity was as high as 35%. C 0.5 exhibited the lowest porosity of 3.7%; however, the porosities in some regions were as high as 20%. These broad porosity distributions indicate a heterogeneous distribution of pores in the 3D space. In contrast, M 0.5, which presented a porosity of 4.2% with a narrower distribution range than the others, indicated that the pore structure was more evenly refined compared with C 0.5. Note that the absolute value of porosity determined in this study does not necessarily represent the actual bulk porosity of the sample, but rather demonstrates relative porosities, as synchrotron X-CT focuses on investigating submicron pores within a limited FOV.

The spatial distribution characteristics of the pores were analyzed using RDFs, as shown in Fig. 21, and the corresponding fitted parameters are summarized in Table 6. Distinct differences in the distribution and organization of the pores were observed among the samples. In the control sample (Fig. 21 (a)), the first peak appeared at a relatively large distance (d=0.76) with a large peak height ($G_r(d)$= 2.29) and a high increasing rate (α=15.21), indicating that pores were distributed with agglomeration [74,106,108,159]. The decay rate (γ) reflected a heterogeneous pore structure; however, it was the lowest among the samples. This was attributed to the abundance of pores in the control sample, which resulted in the repeated existence of mid- and long-range pores, resulting in a partially ordered and correlated pore structure with slow decay.

The RDF of C 0.5 presented a $G_r(d)$ value of 2.28, which is nearly as high as that of the control (Fig. 21 (b)), reflecting a heterogeneously densified microstructure with intensified pore clustering owing to the formation of enlarged calcite crystals [29,160]. The amount of pores in C 0.5 was significantly reduced as shown in the 2D pore images in Fig. 21 (b) and as evidenced in Fig. 19 and Fig. 20, resulting in the fast decay in the RDF (a high γ value of 0.32) owing to the rapid loss of correlation between pores and regularity at mid- and long-range distances.

In comparison with the control and C 0.5, M 0.5 exhibited a notable reduction in the peak height ($G_r(d)$ = 1.49), a shorter first peak evolution distance (d=0.49), and an exceptionally high increasing rate (α=21.39), which indicates comparably less agglomerated distribution of pores and shorter interpore distances (Fig. 21 (c)). Pores were homogeneously distributed but arranged in a highly disordered manner, which resulted in a loss of interpore correlation at shorter distances and a rapid convergence in the RDF (a high γ value of 0.39).

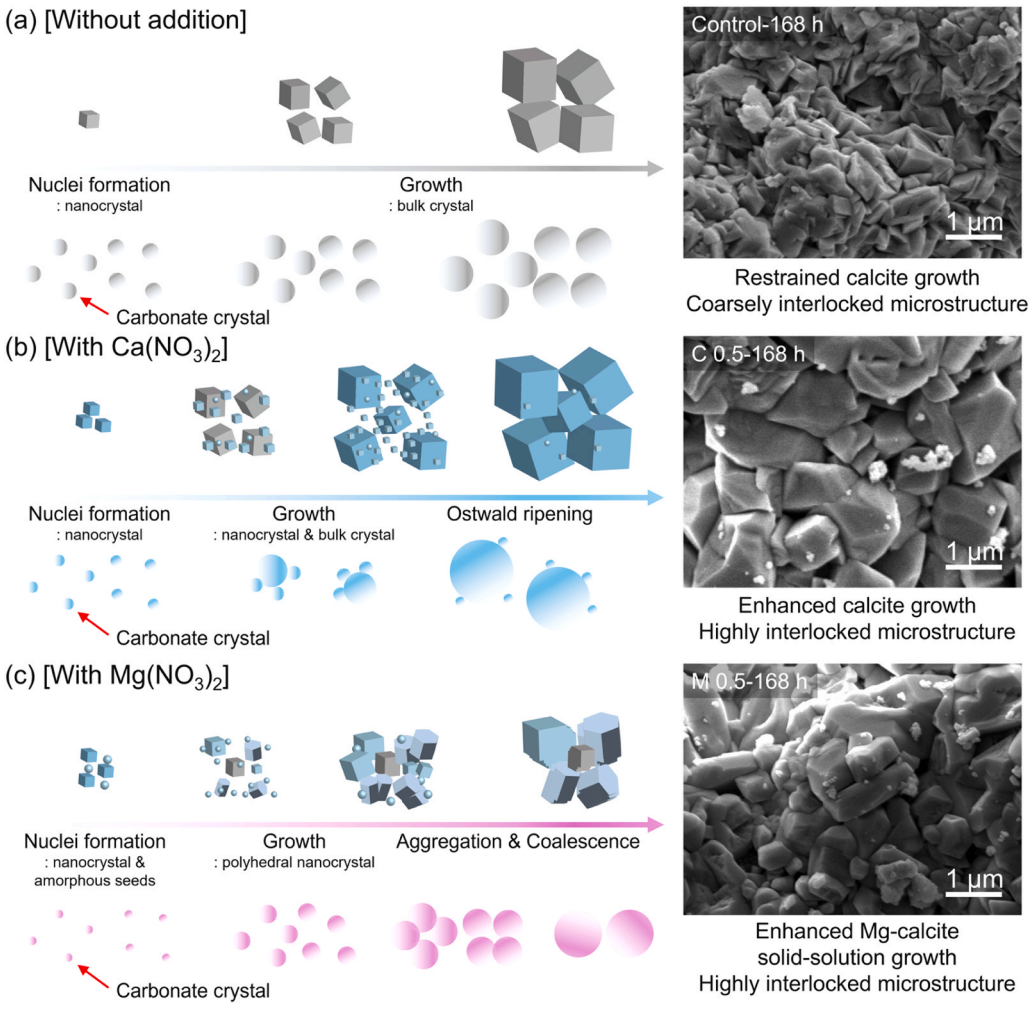

Fig. 18. Changes in the phase formation mechanisms of the LLCs (a) without addition, and with (b) $Ca(NO_3)_2$ and (c) $Mg(NO_3)_2$.

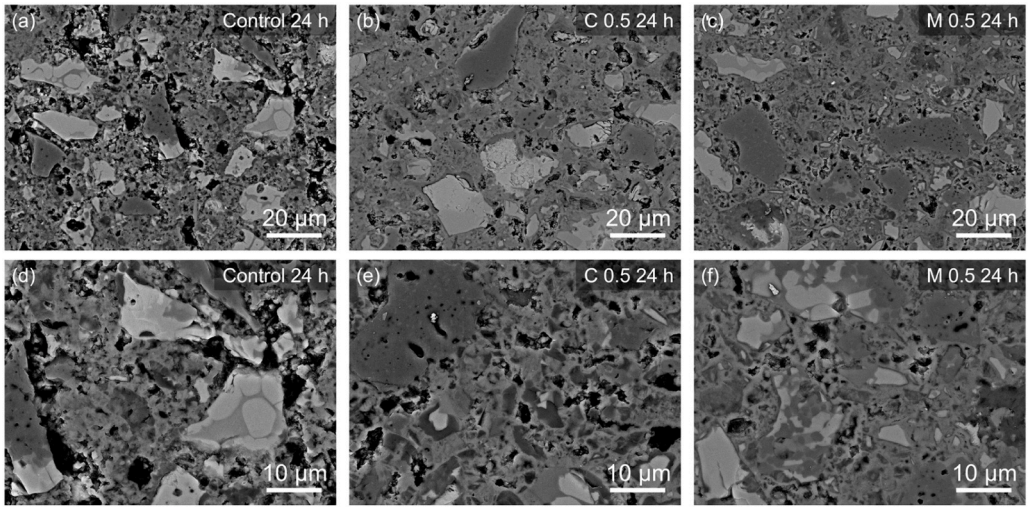

Fig. 19. SEM-BSE images of the LLCs with/without activation obtained at (a)–(c) × 1000 magnification, (d)–(f) × 2000 magnification.

The alterations in the pore shapes of the LLCs induced by $Ca(NO_3)_2$ and $Mg(NO_3)_2$ activation are shown in Fig. 22. The pore shape distribution density plots for the samples are shown in Fig. A4. Fig. 22 (a) shows the 75% contour lines of the distribution density plot of each sample. The contour line of the control group exhibited a shape that was most weighted to the rod-like classification. This can be attributed to the pores generated between the restrictively grown calcite crystals with coarse interlocking. In contrast, both samples activated by $Ca(NO_3)_2$ and $Mg(NO_3)_2$ (C 0.5 and M 0.5) presented distributions that were less biased toward rod-like shapes and shifted toward the other regions. C

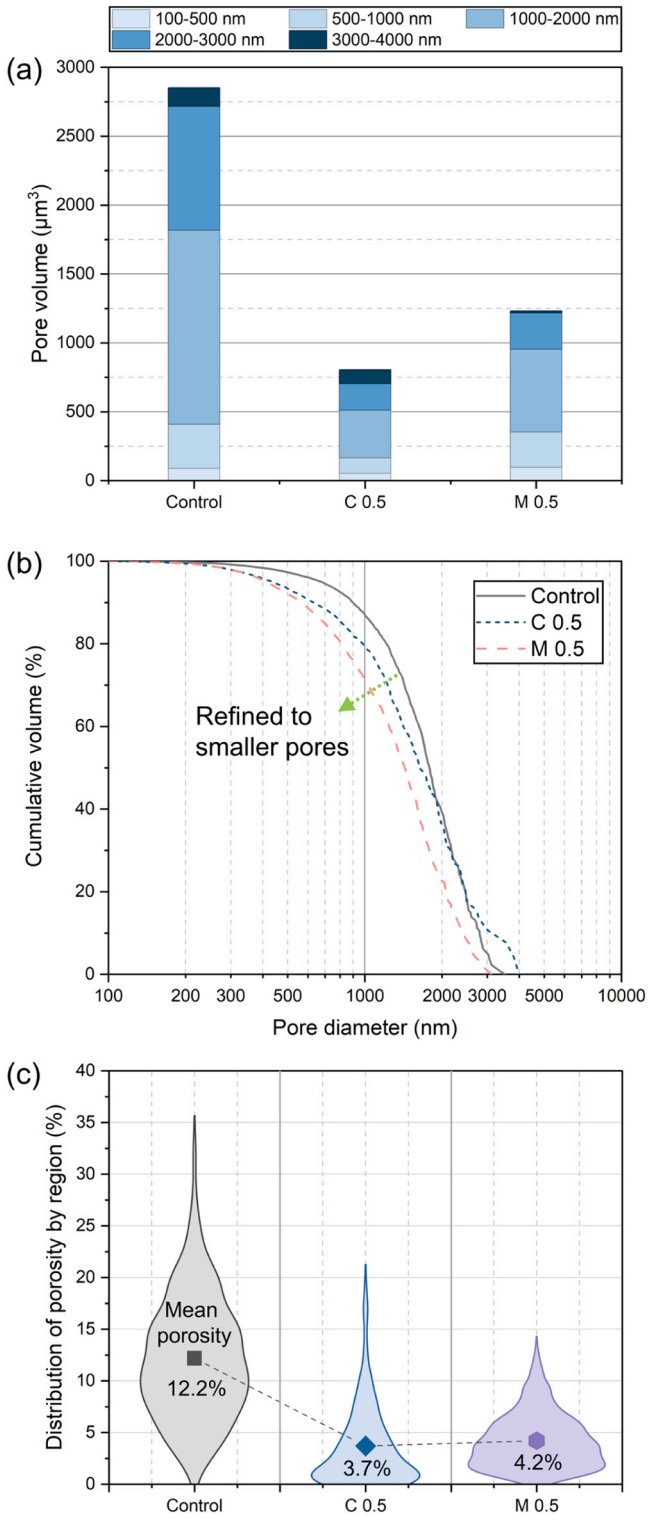

Fig. 20. Porosity refinement of the LLCs activated by $Ca(NO_3)_2$ and $Mg(NO_3)_2$: (a) pore volume by sizes, (b) cumulative pore size distribution, and (c) porosity distribution by regions.

0.5 showed a distribution condensed to a blade-like shape region compared with the control, whereas the distribution of M 0.5 expanded to cuboid-, plate-, and cube-like shape regions and shrank in the blade-like region. This shape alteration can be interpreted through Fig. 22 (b) and (c).

In C 0.5, the enhanced growth of highly angular rhombohedral crystals promoted the formation of blade-like pores owing to the shape of the voids between crystals, as depicted in Fig. 22 (b). Thus, the pores were more likely to be refined to a blade-like shape. However, the polyhedral crystals in M 0.5, which are calcite solid solutions containing Mg^{2+}, left pores of various shapes between the particles, as shown in Fig. 22 (c). This resulted in the broadening of the pore shape distribution of M 0.5, as shown in Fig. 22 (a), toward a wider range of geometric classifications.

Finally, the pore analyses can clarify the interpretation of the mechanical properties. Compared with Control, both activated samples contained substantially less pore volume and fewer connection between the pores. C 0.5 showed the lowest porosity with enlarged rhombohedral calcite crystals and a relatively clustered pore distribution, whereas M 0.5 exhibited smaller pores distributed more uniformly throughout the analyzed volume. The higher strength of C 0.5 despite the greater spatial homogeneity of M 0.5 indicates that uniform pore refinement was not the sole controlling factor. Rather, the larger amount of crystalline carbonate and their pronounced intergrowth in C 0.5 appear to have outweighed the advantage of the more homogeneous pore network in M 0.5. Accordingly, the mechanical performance of CO_2-cured LLC pastes activated by nitrates reflected the combined effects of phase formation, morphological characteristics, and spatial distribution of pores.

3.6. *Implications, limitations, and future perspective*

The present results demonstrate that modification of the initial ionic environment can improve the carbonation performance of LLC without compression molding. Both $Ca(NO_3)_2$ and $Mg(NO_3)_2$ enhanced dissolution and subsequent reaction, while the cation type governed the characteristics of the resulting carbonate phases and microstructures. $Ca(NO_3)_2$ promoted extensive calcite growth and strong crystal interlocking, whereas $Mg(NO_3)_2$ favored the formation of ACC and Mg-calcite, producing a finer and more uniform pore structure. Therefore, the type and concentration of nitrate additives can be selected according to the required balance among reactivity, microstructural development, and mechanical performance. These findings provide a basis for improving CO_2-cured LLC through chemical activation.

To assess the net CO_2 emission considering the increased CO_2 uptake of activated LLCs with the additional emissions associated with nitrate additives, a simplified calculation for emission was calculated as shown in Fig. 23. This calculation excludes transportation, mixing, pre-curing, CO_2 supply, and chamber-operation emissions because these processes were applied identically to all samples and were not quantified at a representative production scale. Hence, the results should be interpreted as a comparative material-level carbon balance rather than a complete life cycle assessment. A corresponding calculation was not conducted for $Mg(NO_3)_2$ because a sufficiently reliable production emission factor was not available from a publicly accessible source. The theoretical CO_2 emission from LLC production was estimated by adapting the equivalent CO_2 calculation proposed by Nie et al. [161] to the chemical composition of the LLC used in this study, assuming its large-scale production in a commercial kiln. The emissions factors of water [162] and $Ca(NO_3)_2$ [163] were adopted and multiplied by the amounts required for each mixture.

The CO_2 uptake measured by TGA after 24 h of curing was converted to the same basis and subtracted from the emissions related to production. The resulting net CO_2 emissions for C 0.1 and C 0.5 were lower than that of Control (48.6 g-CO_2/100 g LLC), reaching 47.4 and 43.0 g-CO2/100 g LLC, respectively. When normalized by compressive strength, C 0.5 exhibited a substantially lower value of 0.34 g-CO_2/100 g LLC/MPa, compared with 1.03 g-CO_2/100 g LLC/MPa for Control. In contrast, excessive nitrate addition at 1.0 M increased the net emissions to 60.4 g-CO_2/100 g LLC for C 1.0 because the additional production burden with the large amount of $Ca(NO_3)_2$ was not compensated by a corresponding increase in CO_2 uptake. These results indicate that an appropriate nitrate dosage can improve both the carbon and mechanical efficiencies of LLC, whereas excessive addition may diminish or reverse the environmental benefit.

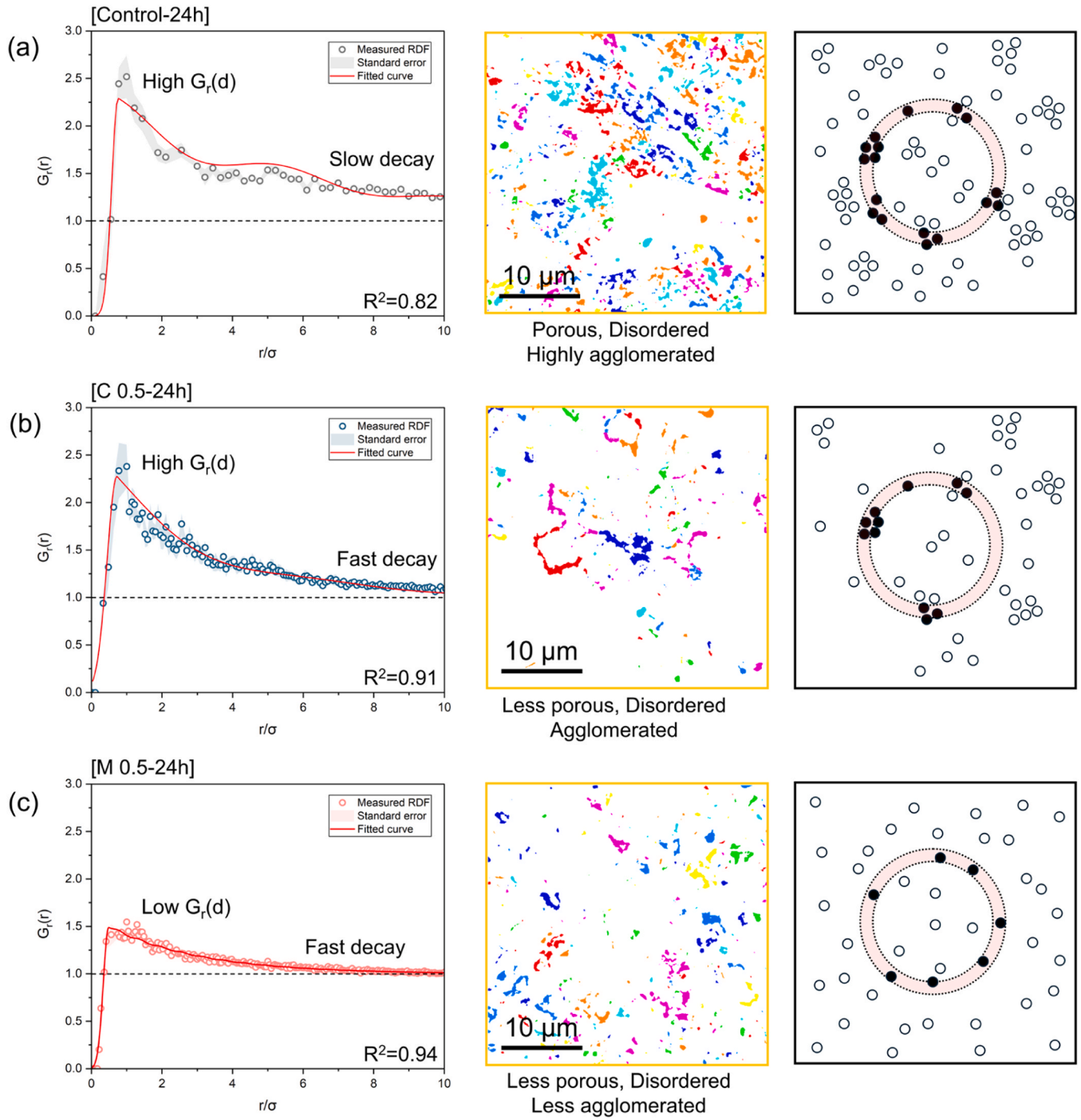

Fig. 21. RDFs of the LLCs activated by $Ca(NO_3)_2$ and $Mg(NO_3)_2$ (a) control, (b) C 0.5, and (c) M 0.5.

Table 6
Fitted parameters of the RDFs.

	d	α	$G_r(d)$	θ	μ	γ
Control	0.76	15.21	2.29	1.29	0.86	0.17
C 0.5	0.73	6.16	2.28	0.98	0.88	0.32
M 0.5	0.49	21.39	1.49	10.56	1.03	0.39

However, the principal limitation of this study is that the size effect was not examined. The specimens used in this study had short transport path which likely contributed to the high DoR and compressive strengths achieved. In larger products, the progression of carbonation inward from the exposed surfaces may generate a dense outer region and a pronounced reaction gradient, thereby restricting further CO_2 penetration. Thus, the absolute values obtained under the present conditions should not be directly perceived as a result directly compatible with large-scale applications. Moreover, the concentration identified as optimal in this study may change with specimen dimensions because the balance among ion dissolution, carbonate precipitation, and CO_2 transport can be altered by the diffusion distance.

Despite this limitation, the extended initial induction observed after nitrate addition (Fig. 16 and Table 5) may provide a meaningful benefit for larger components. The lower reaction constants during Stage I and the substantially higher constants during Stages II and III indicate that

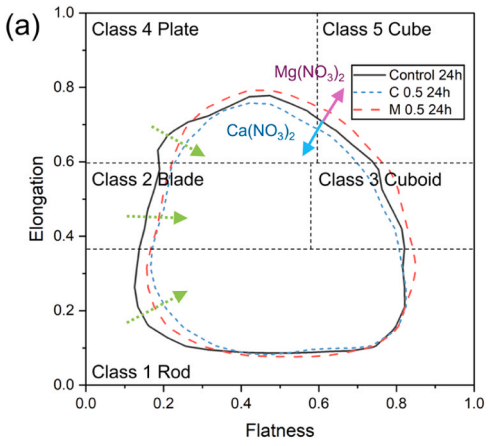

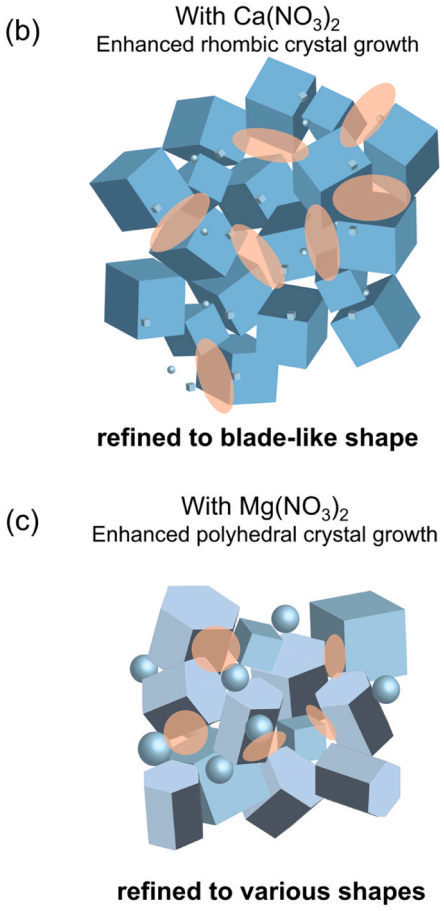

Fig. 22. Pore shape refinement of the LLCs activated by $Ca(NO_3)_2$ and $Mg(NO_3)_2$. (A)Comparison of the 75% distribution density contour lines and shape refinement mechanisms of the LLCs activated by (b) $Ca(NO_3)_2$ and (c) $Mg(NO_3)_2$.

premature formation of the reaction-product barrier was delayed while the subsequent reaction remained active. Moderation of rapid surface precipitation may provide additional time for CO_2 to penetrate toward the interior before substantial densification of the outer region occurs. Future studies should verify this effect using specimens of different dimensions and evaluate the resulting carbonation gradients, spatial phase distributions, CO_2 uptake, and mechanical properties. Such investigations are also required to determine whether the optimum concentrations of $Ca(NO_3)_2$ and $Mg(NO_3)_2$ shift during scale-up.

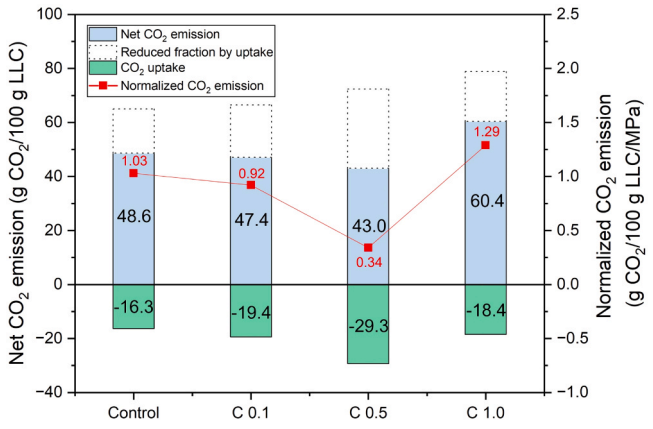

Fig. 23. Simplified net CO_2 emission balance of LLCs CO_2-cured for 24 h.

The practical and environmental implications of nitrate addition should also be considered. $Ca(NO_3)_2$ and $Mg(NO_3)_2$ are commercially available inorganic salts that are produced on a large industrial scale for use in fertilizer and a wide range of other industrial applications [61, 163–165]. Their widespread commercial availability and large-scale production may provide an economic advantage than the other organic additives, such as amino acids or polymeric crystal modifiers, investigated for controlling carbonate precipitation. Therefore, the material cost of nitrate activation may not necessarily represent a major limitation. Nevertheless, the required dosage and the environmental burden associated with nitrate production should be considered when evaluating the net environmental benefit of the proposed activation method. A comprehensive assessment of these factors will require product-scale economic and life cycle analyses.

A further durability consideration concerns the retention and potential leaching of residual nitrate species under humid or water-exposed conditions. Because nitrate salts are highly water-soluble, NO_3^- ions that are not incorporated into solid phases may remain in the pore solution or be weakly adsorbed on the surfaces of unreacted calcium silicates and carbonation products. Consequently, these residual nitrate species may leach from the matrix during prolonged exposure to water. In conventional Portland cement-based systems, nitrate can be incorporated into aluminate hydrates as nitrate-bearing AFm phases, potentially altering the balance among nitrate-, sulfate-, and carbonate-bearing AFm phases and the associated AFm/AFt phase assemblage [166–169]. However, the LLC investigated in this study contained a very low Al content and no detectable crystalline aluminate-bearing phase. Therefore, the formation of substantial amounts of nitrate-AFm and the associated transformation of aluminate hydrates are expected to be limited. Furthermore, the major reaction products were thermodynamically stable $CaCO_3$ phases, and their direct destabilization by residual nitrate or nitrate leaching is considered unlikely. Nevertheless, the progressive removal of soluble nitrate may locally alter the pore solution chemistry, potentially affecting long-term mechanical and microstructural stability. Because residual nitrate content and durability under prolonged exposure to water were not evaluated in this study, such effects cannot be completely excluded. Future studies should therefore quantify nitrate retention and leaching and evaluate the corresponding changes in strength, pore structure, and phase assemblage after prolonged immersion and repeated exposure. This issue may require particular attention for LLCs produced from natural raw materials with higher Al contents, in which nitrate-bearing AFm formation and changes in the AFm/AFt balance may become significant.

4. Conclusion

This study investigated the comparative effects of $Ca(NO_3)_2$ and $Mg(NO_3)_2$ on the CO_2-curing of LLCs, distinguishing their roles in the

dissolution, reaction kinetics, phase evolution, and microstructural development. These results demonstrated that the incorporation of both nitrates fundamentally enhanced the reaction, with varying effects depending on the type of cation (Ca^{2+} and Mg^{2+}). The detailed conclusions are as follows.

- The addition of both $Ca(NO_3)_2$ and $Mg(NO_3)_2$ markedly altered the early chemical environment of the LLCs by increasing Ca release through enhanced ionic strength. At 0.5 M, which provided the highest performance among the concentrations examined under the present conditions, $Ca(NO_3)_2$ led to the extensive formation of crystalline calcite through Ostwald ripening, whereas $Mg(NO_3)_2$ promoted the formation of ACC and Mg-calcite through particle aggregation, resulting in different carbonation products depending on the cation type.
- The highest reaction rate and DoR were obtained at 0.5 M for both additives. $Mg(NO_3)_2$ enhanced the reactivity over a wider concentration range, whereas $Ca(NO_3)_2$ exhibited a narrower effective concentration range. Reaction kinetics modelling revealed that both nitrate additives improved the carbonation progress by mitigating premature reactions and sustaining reactivity after the initial stage through an extended induction period, which contributed to the enhanced dissolution of Ca^{2+}.
- The distinct carbonate products induced by $Ca(NO_3)_2$ and $Mg(NO_3)_2$ resulted in different pore structures. $Ca(NO_3)_2$ resulted in densely interlocked calcite crystals of broad sizes, whereas $Mg(NO_3)_2$ generated finer and more uniformly distributed carbonate phases, producing a refined pore network with reduced clustering and a smaller pore size.
- The changes in phase formation and pore structure directly improved the compressive strength and CO_2 uptake. Both additives significantly enhanced the mechanical performance of the LLCs (128 MPa for $Ca(NO_3)_2$ and 112 MPa for $Mg(NO_3)_2$) with 0.5 M activation. $Ca(NO_3)_2$ achieved higher strength through extensive calcite formation despite the heterogeneous pore structure, whereas $Mg(NO_3)_2$ provided a comparable but lower improvement than $Ca(NO_3)_2$ through effective pore refinement and uniform carbonate distribution. Notably, the extensive mechanical interlocking between the $CaCO_3$ crystals was more decisive than the homogeneous pore structure for the strength development of the CO_2-cured LLCs.

These findings provide critical insights into how Ca^{2+}- and Mg^{2+}-based additives regulate dissolution, carbonation kinetics, and product formation in LLCs, which are crucial for improving both carbon uptake efficiency and mechanical performance. By identifying the proper additive concentration and clarifying the distinct roles of $Ca(NO_3)_2$ and $Mg(NO_3)_2$, this study demonstrated that the targeted modification of the early ionic environment can substantially enhance the performance of carbonation-activated cementitious materials. These results establish a robust basis for developing LLC-based materials with improved material efficiency and mechanical properties through chemical activation, thereby supporting their practical application in sustainable construction.

Declaration of Competing InterestThe authors declare that they have no known competing financial interests or personal relationships that could have appeared to influence the work reported in this paper.

CRediT authorship contribution statement

Seongmin Cho: Writing – review & editing, Writing – original draft, Visualization, Validation, Software, Methodology, Investigation, Formal analysis, Data curation, Conceptualization. **Heongwon Suh:** Writing – review & editing, Validation, Methodology, Investigation. **Sungwon Sim:** Writing – review & editing, Methodology, Investigation. **Jihwan Yang:** Writing – review & editing, Methodology. **Taiyan Piao:** Writing – review & editing, Methodology, Investigation. **Peiqi Li:** Writing – review & editing, Methodology, Investigation. **Sungchul Bae:** Writing – original draft, Validation, Supervision, Resources, Project administration, Investigation, Funding acquisition.

Declaration of Competing Interest

The authors declare that they have no known competing financial interests or personal relationships that could have appeared to influence the work reported in this paper.

Acknowledgement

This work was supported by the Technology Innovation Program-"Development of production technology for 10 ton/batch grade cement products using calcium silicate cement (grant number RS-2022–00155521)" funded by the Ministry of Trade, Industry & Resources (MOTIR, Korea).

Appendix

Eq. A1. **Determination of free water content after pre-curing**

$$Water\ content = (W_{pre-curing} - W_{dry})/W_{pre-curing}, \tag{A1}$$

where *Water content*, $W_{pre-curing}$, and W_{dry} denote the the free water content in the LLC paste, the weight of paste immediately after pre-curing, and the weight of pastes after drying, respectively.

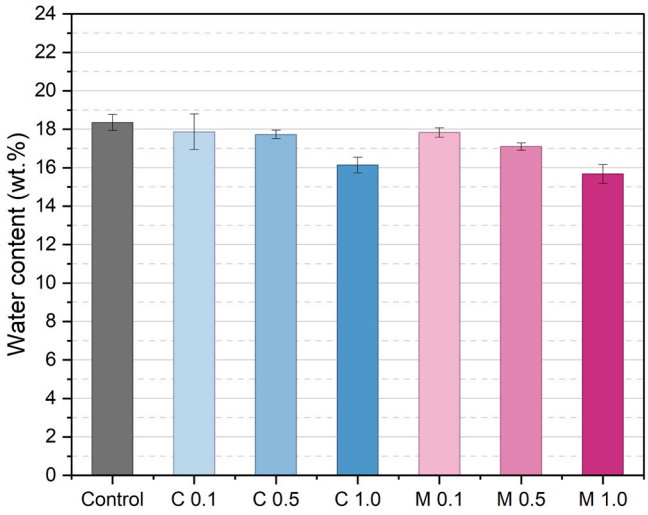

Fig. A1. Amount of free water in the LLC pastes after pre-curing (before CO_2 curing)

Table A1
Rwp values of the phase quantification by Rietveld analysis

Curing time	Samples (5 × 5 × 10 mm blocks)						
	Control	C 0.1	C 0.5	C 1.0	M 0.1	M 0.5	M 1.0
Raw LLC	8.15						
After pre-curing (before CO_2)	7.94	7.64	7.61	7.86	7.93	7.77	7.57
3 h	6.48	6.52	6.40	6.88	6.39	6.37	6.23
6 h	6.43	6.76	6.37	6.73	6.27	5.98	6.09
24 h	6.37	6.48	6.40	6.30	6.18	6.01	5.97
Curing time	Samples (Reaction kinetics)						
	Control		C 0.5			M 0.5	
1 min	7.78		7.56			7.82	
3 min	7.70		7.35			7.65	
10 min	7.69		7.57			7.84	
30 min	7.64		7.45			8.02	
60 min	7.56		7.51			7.33	
90 min	7.53		7.55			7.42	
120 min	7.45		7.73			7.12	
180 min	7.40		7.76			7.47	
360 min	7.45		7.58			7.63	
1440 min	7.75		8.53			7.67	
3600 min	7.43		8.66			7.64	
10080 min	7.53		8.68			7.63	

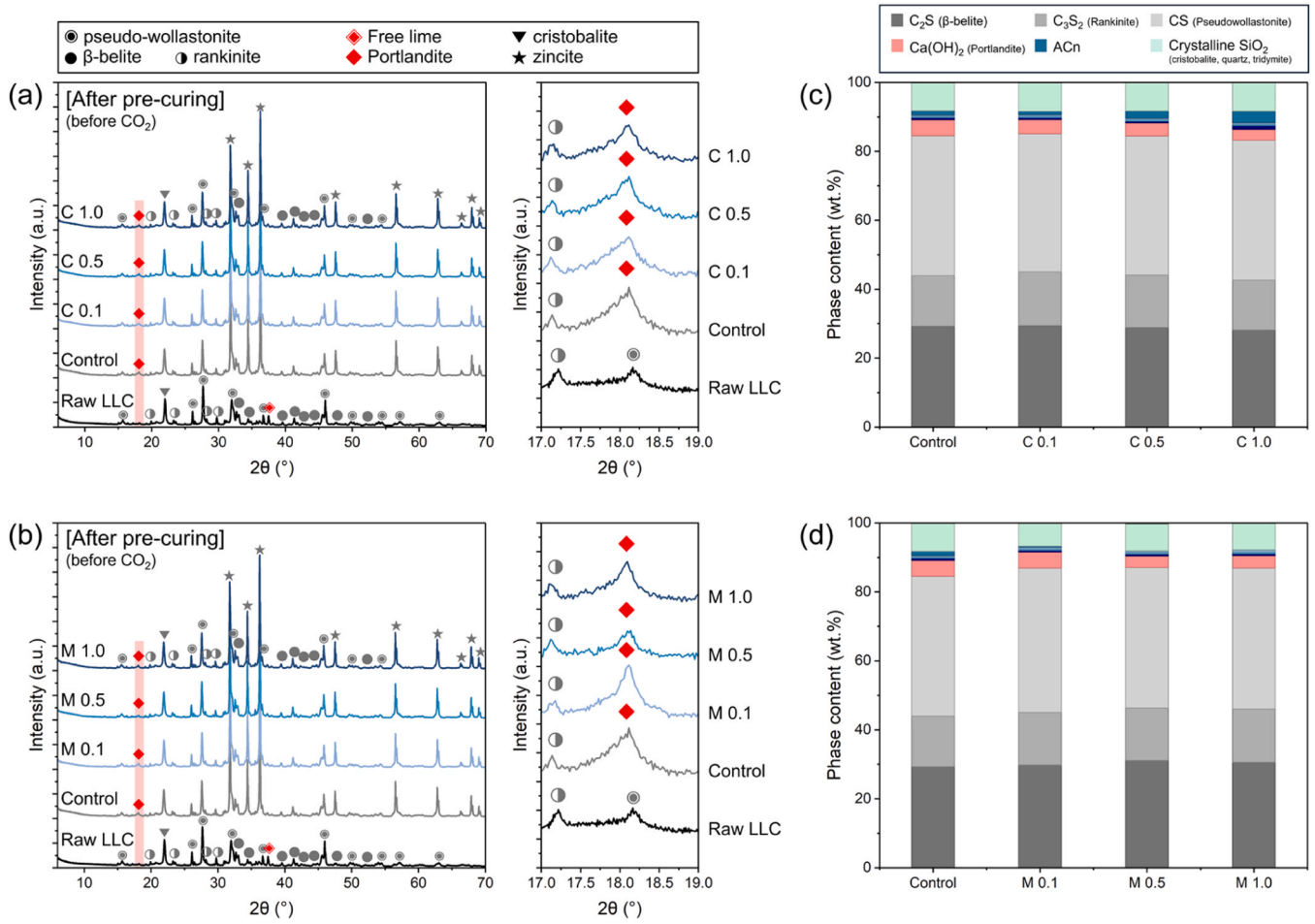

Fig. A2. Crystalline phase analysis of LLCs after pre-curing: XRD spectra ((a) and (b)); and Quantified phase content (c) and (d))

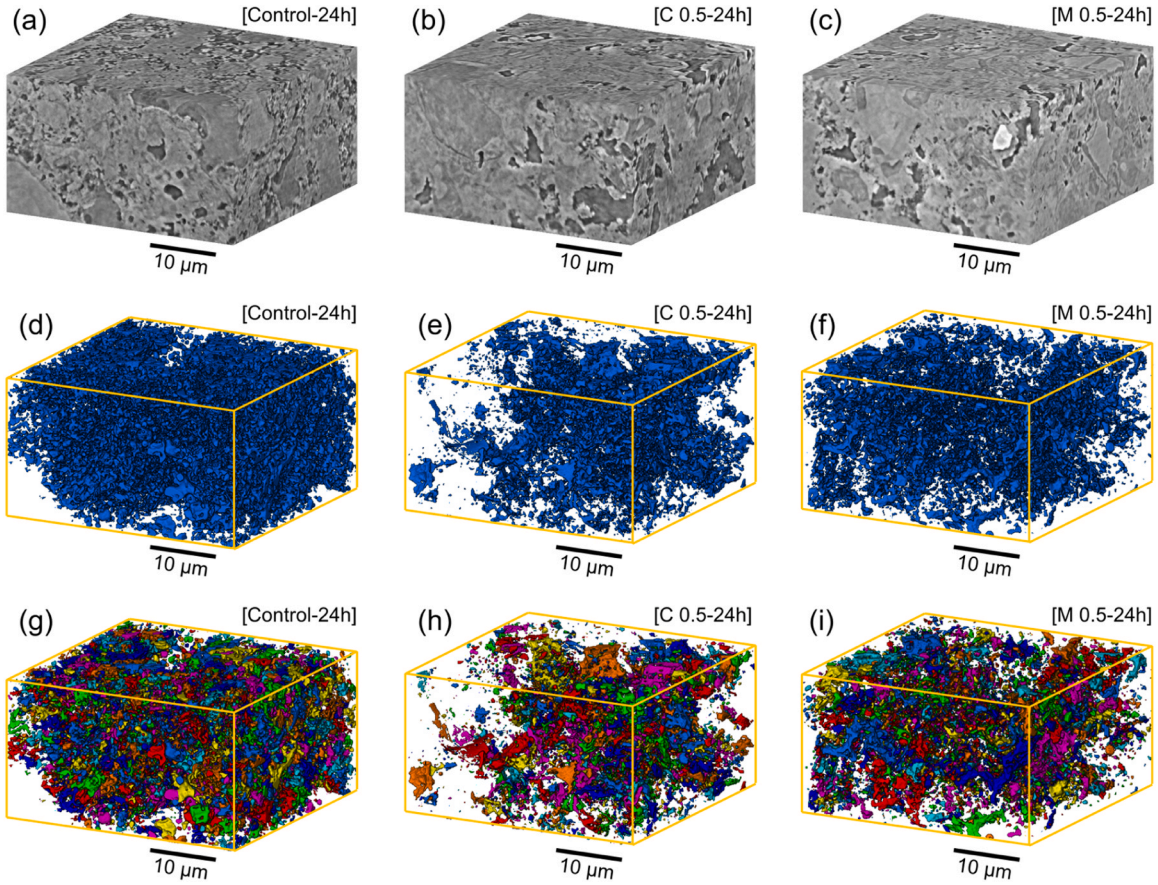

Fig. A3. 3D reconstructed microstructure of LLC pastes CO_2-cured for 24 h: (a)–(c) Grayscale matrix, (d)–(f) thresholded pores, and (g)–(i) separated individual pores

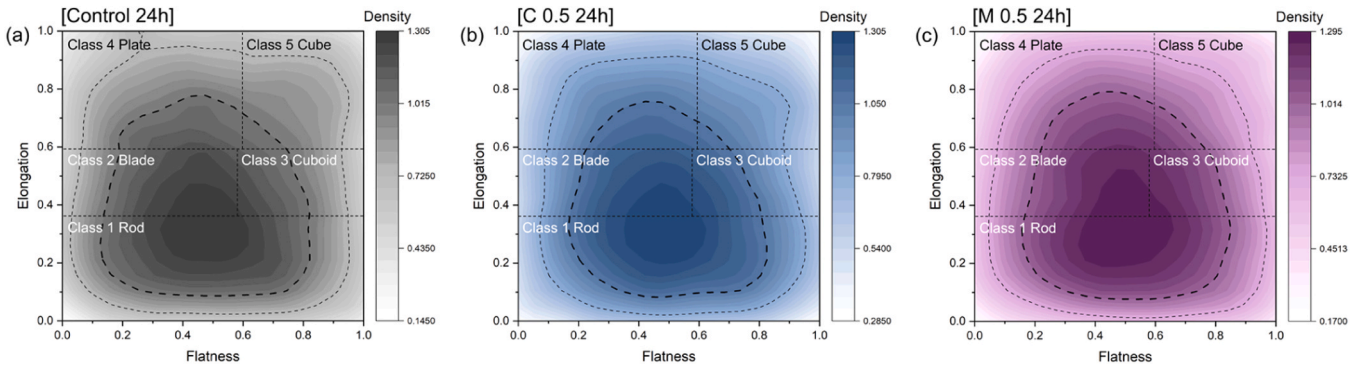

Fig. A4. kernel density plot for the pore shape classification of (a) Control, (b) C 0.5, and (c) M 0.5

Data availability

Data will be made available on request.

References

[1] IPCC, Climate Change 2022: Mitigation of Climate Change, Cambridge University Press, Cambridge, UK and New York, NY, USA, 2022, https://doi.org/10.1017/9781009157926.
[2] 2024, USGeologicalSurvey, Mineral commodity summaries 2024, Mineral Commodity Summaries, Reston, VA,(2024), p. 212. https://doi.org/10.3133/mcs.
[3] 2024, IEA, Breakthrough Agenda Report 2024, Paris, (2024). https://www.iea.org/reports/breakthrough-agenda-report.
[4] 2024, WorldEconomicForum, Nature Positive: Role of the Cement and Concrete Sector., (2024). https://www.weforum.org/publications/nature-positive-transitions-sectors/cement-and-concrete-sector/.
[5] P.C.A. Roadmap, to Carbon Neurality, PCA (Portland Cement Association), Skokie (2021).
[6] M.N. Seifu, J.K. Adem, H.R. Khalid, G.M. Kim, S. Park, Effects of water-to-binder ratios on the workability, durability and strength development of in-situ carbonated concrete, Int. J. Concr. Struct. Mater. 19 (2025) 96, https://doi.org/10.1186/s40069-025-00827-8.
[7] H. Song, M. Oh, I. Kim, B.-G. Son, H.-S. Lee, W.S. Yum, H. Song, Homogenization of metastable chlorine by-pass dust through mineral carbonization, Int. J. Concr. Struct. Mater. 20 (2026) 31, https://doi.org/10.1186/s40069-025-00884-z.
[8] T. Ali, M.S. Mahmood, H. Ahmed, M.Z. Qureshi, K.M. Elhadi, G.U. Alaneme, M. S. Kırgız, A. Ajwad, Accelerated carbonation techniques of recycled concrete aggregates: a systematic review of methods, effects, and optimal conditions, Int. J. Concr. Struct. Mater. 20 (2026) 30, https://doi.org/10.1186/s40069-026-00907-3.

[9] D. Zhang, Z. Ghouleh, Y.X. Shao, Review on carbonation curing of cement-based materials, J. CO2. Util. 21 (2017) 119–131, https://doi.org/10.1016/j.jcou.2017.07.003.
[10] Z. Liu, W.N. Meng, Fundamental understanding of carbonation curing and durability of carbonation-cured cement-based composites: a review, J. CO2. Util. 44 (2021) 101428, https://doi.org/10.1016/j.jcou.2020.101428.
[11] B. Liu, J. Qin, J. Shi, J. Jiang, X. Wu, Z. He, New perspectives on utilization of CO2 sequestration technologies in cement-based materials, Constr. Build. Mater. 272 (2021) 121660, https://doi.org/10.1016/j.conbuildmat.2020.121660.
[12] S. Han, J.H. Kim, R.K. Singh, S.P. Shah, CO2 utilization for cementitious materials - A review, Ksce. J. Civil. Eng. 29 (2025) 100227, https://doi.org/10.1016/j.kscej.2025.100227.
[13] R. Fan, J. Huang, Y. Pei, W. Zhao, X. Ou, Q. Su, H. Yao, Y. Shang, A. Luo, Multiscale Mechanisms Governing the Performance Evolution of MgO-GGBS-Stone Powder Lightweight Foamed Soil Under CO2 Curing, Int. J. Concr. Struct. Mater. 20 (2026) 70, https://doi.org/10.1186/s40069-026-00939-9.
[14] B. Šavija, M. Luković, Carbonation of cement paste: Understanding, challenges, and opportunities, Constr. Build. Mater. 117 (2016) 285–301, https://doi.org/10.1016/j.conbuildmat.2016.04.138.
[15] J.G. Jang, G.M. Kim, H.J. Kim, H.K. Lee, Review on recent advances in CO2 utilization and sequestration technologies in cement-based materials, Constr. Build. Mater. 127 (2016) 762–773, https://doi.org/10.1016/j.conbuildmat.2016.10.017.
[16] J. Ye, J. Fang, Y. Sun, X. Shi, G. Chen, T. Ma, X. Zhi, CO2 mineralization of cement-based materials by accelerated CO2 mineralization and its mineralization degree: A review, Constr. Build. Mater. 444 (2024) 137712, https://doi.org/10.1016/j.conbuildmat.2024.137712.
[17] A. Smigelskyte, R. Siauciunas, H. Hilbig, M. Decker, L. Urbonas, G. Skripkiunas, Carbonated rankinite binder: effect of curing parameters on microstructure, strength development and durability performance, Sci. Rep. 10 (2020) 14462, https://doi.org/10.1038/s41598-020-71270-w.
[18] Y. Mu, Z. Liu, F. Wang, Comparative Study on the Carbonation-Activated Calcium Silicates as Sustainable Binders: Reactivity, Mechanical Performance, and Microstructure, ACS Sustain. Chem. Eng. 7 (2019) 7058–7070, https://doi.org/10.1021/acssuschemeng.8b06841.
[19] W. Ashraf, J. Olek, V. Atakan, Carbonation reaction kinetics, CO2 sequestration capacity, and microstructure of hydraulic and non-hydraulic cementitious binders, Proc. Fourth Int. Conf. Sustain. Constr. Mater. Technol. (2016) 7–11, https://doi.org/10.18552/2016/SCMT4S303.
[20] W. Ashraf, J. Olek, Carbonation behavior of hydraulic and non-hydraulic calcium silicates: potential of utilizing low-lime calcium silicates in cement-based materials, J. Mater. Sci. 51 (2016) 6173–6191, https://doi.org/10.1007/s10853-016-9909-4.
[21] J.K. Adem, J. Seo, S. Park, G.M. Kim, Effects of low-lime calcium silicate cement addition on the hydration, carbonation, and microstructural characteristics of OPC pastes by carbonation curing, J. Build. Eng. 107 (2025) 112683, https://doi.org/10.1016/j.jobe.2025.112683.
[22] S. Tamta, R. Chaudhury, U. Sharma, M. Hanifa, P.C. Thapliyal, L.P. Singh, Low lime – low carbon cement: Achieving sustainability through reduction of CO2 emissions and utilizing limestone mining rejects, Constr. Build. Mater. 470 (2025) 140476, https://doi.org/10.1016/j.conbuildmat.2025.140476.
[23] Y. Fang, Z. Liu, Q. Wang, Y. Zhang, M. Zhang, Q. Wang, Strength Development and Products Evolution of β-C2S and γ-C3S Induced by Accelerated Carbonation Curing, J. Wuhan. Univ. Technol. Mater. Sci. Ed. 35 (2020) 1053–1060, https://doi.org/10.1007/s11595-020-2355-9.
[24] C. Li, B. Liu, Q. Zheng, Y. Li, X. Zhu, Y. Fang, Q. Zhao, Z. Jiang, J. Li, Carbonation reactivity of calcium silicate glasses at various calcium to silicate ratios and comparison with wollastonite, Cem. Concr. Res. 186 (2024) 107653, https://doi.org/10.1016/j.cemconres.2024.107653.
[25] S. Liu, Y. Sun, G. Li, J. Zhu, X. Guan, Z. Liu, F. Wang, A comprehensive review of calcium metasilicate(CaSiO3) polymorphs as low-carbon cementitious materials for CO2 sequestration, J. Build. Eng. 111 (2025) 113248, https://doi.org/10.1016/j.jobe.2025.113248.
[26] S. Zhao, Z. Liu, F. Wang, S. Hu, Elucidating factors on the strength of carbonated compacts: Insights from the carbonation of γ-C2S, β-C2S and C3S, Cem. Concr. Compos. 155 (2025) 105806, https://doi.org/10.1016/j.cemconcomp.2024.105806.
[27] S. Goto, K. Suenaga, T. Kado, M. Fukuhara, Calcium Silicate Carbonation Products, J. Am. Ceram. Soc. 78 (1995) 2867–2872, https://doi.org/10.1111/j.1151-2916.1995.tb09057.x.
[28] S. Cho, H. Suh, G. Kim, J. Liu, P. Li, S. Bae, Microstructural phase evolution and strength development of low-lime calcium silicate cement (CSC) paste incorporating ordinary Portland cement under an accelerated carbonation curing environment, Constr. Build. Mater. 411 (2024) 134248, https://doi.org/10.1016/j.conbuildmat.2023.134248.
[29] S. Cho, H. Suh, J. Park, S. Jeong, J. Park, S. Bae, Repetitive water replenishment in CO2 curing: Enhancement in carbon uptake, reactivity, crystal development, and mechanical properties of low calcium binder composites, Cem. Concr. Compos. 160 (2025) 106053, https://doi.org/10.1016/j.cemconcomp.2025.106053.
[30] Z. Zhang, K. Zheng, L. Chen, Q. Yuan, Review on accelerated carbonation of calcium-bearing minerals: Carbonation behaviors, reaction kinetics, and carbonation efficiency improvement, J. Build. Eng. 86 (2024) 108826, https://doi.org/10.1016/j.jobe.2024.108826.
[31] Z. Liu, C. Lv, F. Wang, S. Hu, Recent advances in carbonatable binders, Cem. Concr. Res. 173 (2023) 107286, https://doi.org/10.1016/j.cemconres.2023.107286.
[32] A. Bersisa, K.-Y. Moon, G.M. Kim, J.-S. Cho, S. Park, Influence of hydraulic cement substitutes on carbonation of calcium silicate cement, Constr. Build. Mater. 473 (2025) 140800, https://doi.org/10.1016/j.conbuildmat.2025.140800.
[33] Z. Zhang, K. Zheng, L. Chen, Q. Yuan, Enhancing carbonation-activated γ-C2S compacts through Na2CO3 post-curing: Alkalinity and mechanical properties improvement, J. Build. Eng. 103 (2025) 112136, https://doi.org/10.1016/j.jobe.2025.112136.
[34] Y. Mu, Z. Liu, F. Wang, X. Huang, Carbonation characteristics of γ-dicalcium silicate for low-carbon building material, Constr. Build. Mater. 177 (2018) 322–331, https://doi.org/10.1016/j.conbuildmat.2018.05.087.
[35] X. Du, J. Chang, L. Lin, X. Peng, H. Han, Y. Bai, Performance differences and mechanism of carbonation-hardened compacts produced with different C2S polymorphs: A new perspective of carbonatable binder, Cem. Concr. Compos. 163 (2025) 106216, https://doi.org/10.1016/j.cemconcomp.2025.106216.
[36] Y.S. Han, G. Hadiko, M. Fuji, M. Takahashi, Crystallization and transformation of vaterite at controlled pH, J. Cryst. Growth 289 (2006) 269–274, https://doi.org/10.1016/j.jcrysgro.2005.11.011.
[37] Y.I. Svenskaya, H. Fattah, O.A. Inozemtseva, A.G. Ivanova, S.N. Shtykov, D. A. Gorin, B.V. Parakhonskiy, Key parameters for size-and shape-controlled synthesis of vaterite particles, Cryst. Growth Des. 18 (2018) 331–337, https://doi.org/10.1021/acs.cgd.7b01328.
[38] M. Kogo, T. Umegaki, Y. Kojima, Effect of pH on formation of single-phase vaterite, J. Cryst. Growth 517 (2019) 35–38, https://doi.org/10.1016/j.jcrysgro.2019.04.005.
[39] G. Li, S. Liu, X. Hu, J. Zhu, X. Guan, C. Shi, Effect of pH environment on carbonation properties of γ-C2S, Constr. Build. Mater. 461 (2025) 139888, https://doi.org/10.1016/j.conbuildmat.2025.139888.
[40] Z. Xu, L. Yu, B. Lu, J. Sun, Z. Liu, H.M. Naguib, G. Hou, Aragonite formation induced by triethylene glycol and its enhancement to flexural strength in carbonated rankinite cement, Constr. Build. Mater. 408 (2023) 133514, https://doi.org/10.1016/j.conbuildmat.2023.133514.
[41] A. Bersisa, K.-Y. Moon, G.M. Kim, J.-S. Cho, S. Park, Internal carbonation of calcium silicate cement incorporated with Na2CO3 and NaHCO3, Constr. Build. Mater. 462 (2025) 139732, https://doi.org/10.1016/j.conbuildmat.2024.139732.
[42] J. Zhu, J. Cao, G. Li, Y. Bian, The effects of Mg(NO3)2 on the carbonation properties of the Low Calcium Carbonatable Binder, Constr. Build. Mater. 477 (2025) 141331, https://doi.org/10.1016/j.conbuildmat.2025.141331.
[43] Y. Liang, Y. Liu, Z. Liu, F. Wang, S. Hu, Enhancement of flexural strength of γ-C2S carbonated compacts through in situ synthesis of Mg-calcite, Compos. B Eng. 297 (2025) 112331, https://doi.org/10.1016/j.compositesb.2025.112331.
[44] P. Rong, S. Liu, R. Li, S. Zhang, H. Guo, X. Guan, J. Zhu, C. Shi, Enhancing the carbonation of γ-C2S through MgCl2 incorporation, Constr. Build. Mater. 409 (2023) 134138, https://doi.org/10.1016/j.conbuildmat.2023.134138.
[45] F. Wu, X. You, M. Wang, T. Liu, B. Lu, G. Hou, R. Jiang, C. Shi, Increasing flexural strength of CO2 cured cement paste by CaCO3 polymorph control, Cem. Concr. Compos. 141 (2023) 105128, https://doi.org/10.1016/j.cemconcomp.2023.105128.
[46] S. Zhang, O. Nahi, L. Chen, Z. Aslam, N. Kapur, Y.-Y. Kim, F.C. Meldrum, Magnesium Ions Direct the Solid-State Transformation of Amorphous Calcium Carbonate Thin Films to Aragonite, Magnesium-Calcite, or Dolomite, Adv. Funct. Mater. 32 (2022) 2201394, https://doi.org/10.1002/adfm.202201394.
[47] J.S. Ndzila, Z. Yang, Carbonation properties of ion-doped non-hydraulic calcium silicate binders: A review, J. Build. Eng. 105 (2025) 112427, https://doi.org/10.1016/j.jobe.2025.112427.
[48] J. Huang, Y. Chen, Q. Yu, Bioinspired calcium carbonate binders via synergistic crystallization control of amorphous calcium carbonate using poly aspartic acid and magnesium ions, Constr. Build. Mater. 506 (2026) 144924, https://doi.org/10.1016/j.conbuildmat.2025.144924.
[49] S. Tamta, R. Chaudhury, A. Bohra, U. Sharma, P.C. Thapliyal, L.P. Singh, Studies on mineralogy and carbonation kinetics of low-lime low-carbon cement by substituting magnesia and alumina, Constr. Build. Mater. 521 (2026) 145887, https://doi.org/10.1016/j.conbuildmat.2026.145887.
[50] P. Shen, J. Lu, Y. Zhang, Y. Jiang, S. Zhang, C.S. Poon, Preparation aragonite whisker-rich materials by wet carbonation of cement: Towards yielding micro-fiber reinforced cement and sequestrating CO2, Cem. Concr. Res. 159 (2022) 106891, https://doi.org/10.1016/j.cemconres.2022.106891.
[51] D. Zhong, W. Zhang, S. Zhang, G. Hou, B. Lu, Preparation of aragonite whisker-rich materials by wet carbonation of magnesium slag: A sustainable approach for CO2 sequestration and reinforced cement, Constr. Build. Mater. 418 (2024) 135429, https://doi.org/10.1016/j.conbuildmat.2024.135429.
[52] Z. Huo, B. Lu, J. Sun, R. Jiang, G. Hou, S. Ji, H.M. Naguib, Preparation of high flexural strength rankinite cement benefiting from formation of aragonite whisker during carbonation curing, J. Sustain. Cem. -Based Mater. 13 (2024) 738–753, https://doi.org/10.1080/21650373.2024.2302095.
[53] L. Yang, Z. Liu, P. Rong, S. Luo, X. Guan, J. Zhu, X. Zhou, S. Liu, G. Li, Optimizing carbonation efficiency and mechanical properties of low-calcium cementitious materials with MgSO4 addition, Constr. Build. a, Constr. Build. Mater. Mater. 454 (2024) 139148, https://doi.org/10.1016/j.conbuildmat.2024.139148.
[54] S. Cho, S. Jeong, J. Park, S. Bae, Enhanced reactivity and CO2 mineralization of low-lime calcium silicate cement by incorporating nitric acid as an initial calcium

leaching agent, J. CO2. Util. 86 (2024) 102913, https://doi.org/10.1016/j.jcou.2024.102913.
[55] J.D. Rodriguez-Blanco, S. Shaw, L.G. Benning, The kinetics and mechanisms of amorphous calcium carbonate (ACC) crystallization to calcite, via vaterite, Nanoscale 3 (2011) 265–271, https://doi.org/10.1039/c0nr00589d.
[56] D. Zhao, J.M. Williams, P. Hou, A.J. Moment, S. Kawashima, Stabilizing mechanisms of metastable vaterite in cement systems, Cem. Concr. Res. 178 (2024) 107441, https://doi.org/10.1016/j.cemconres.2024.107441.
[57] T. Oey, J. Stoian, J. Li, C. Vong, M. Balonis, A. Kumar, W. Franke, G. Sant, Comparison of $Ca(NO_3)_2$ and $CaCl_2$ Admixtures on Reaction, Setting, and Strength Evolutions in Plain and Blended Cementing Formulations, J. Mater. Civ. Eng. 27 (2015) 04014267, https://doi.org/10.1061/(ASCE)MT.1943-5533.0001240.
[58] Q. Li, Y. Wang, G. Geng, H. Chen, P. Hou, X. Cheng, P.J.M. Monteiro, S. Huang, J. H. Kim, Microstructural Study of Hydration of C3S in the Presence of Calcium Nitrate Using Scanning Transmission X-Ray Microscopy (STXM), J. Nanomater. 2020 (2020) 8419130, https://doi.org/10.1155/2020/8419130.
[59] Q. Li, Y. Ge, G. Geng, S. Bae, P.J.M. Monteiro, CaCl2-Accelerated Hydration of Tricalcium Silicate: A STXM Study Combined with 29Si MAS NMR, J. Nanomater. 2015 (2015) 215371, https://doi.org/10.1155/2015/215371.
[60] J.J. Thomas, A.J. Allen, H.M. Jennings, Hydration Kinetics and Microstructure Development of Normal and CaCl2-Accelerated Tricalcium Silicate Pastes, J. Phys. Chem. C. 113 (2009) 19836–19844, https://doi.org/10.1021/jp907078u.
[61] S. Kant, U. Kafkafi, Fertigation. Encyclopedia of Soils in the Environment, Elsevier, 2013.
[62] X. Yin, D. Li, Y. Tan, X. Wu, X. Yu, D. Zeng, Solubility Phase Diagram of the Ca (NO3)2–Mg(NO3)2−H2O System, J. Chem. Eng. Data. 59 (2014) 4026–4030, https://doi.org/10.1021/je500629s.
[63] I. Galan, L. Perron, F.P. Glasser, Impact of chloride-rich environments on cement paste mineralogy, Cem. Concr. Res. 68 (2015) 174–183, https://doi.org/10.1016/j.cemconres.2014.10.017.
[64] S. Chatterji, Mechanism of the CaCl2 attack on portland cement concrete, Cem. Concr. Res. 8 (1978) 461–467, https://doi.org/10.1016/0008-8846(78)90026-1.
[65] A. Bersisa, K.-Y. Moon, G.M. Kim, J.-S. Cho, S. Park, Microstructural characterization of CO2-cured calcium silicate cement, Dev. Built Environ. 19 (2024) 100518, https://doi.org/10.1016/j.dibe.2024.100518.
[66] W. Ashraf, J. Olek, S. Sahu, Phase evolution and strength development during carbonation of low-lime calcium silicate cement (CSC), Constr. Build. Mater. 210 (2019) 473–482, https://doi.org/10.1016/j.conbuildmat.2019.03.038.
[67] J.-H. Kim, A. Berhanu Degefa, S.-A. Jo, A. Salas Montoya, C.-W. Chung, Effect of heat treatment on bentonites for utilization as a supplementary cementitious material, J. Strcut. Integ. 11 (2026) 2609326, https://doi.org/10.1080/24705314.2025.2609326.
[68] W.S. Yum, J.-I. Suh, S. Sim, S. Yoon, Y. Jun, J.E. Oh, Influence of calcium and sodium nitrate on the strength and reaction products of the CaO-activated GGBFS system, Constr. Build. Mater. 215 (2019) 839–848, https://doi.org/10.1016/j.conbuildmat.2019.04.240.
[69] C. Sigtryggsson, K. Hamnér, H. Kirchmann, Laboratory studies on dissolution of nitrogen fertilizers by humidity and precipitation, Agric. Environ. Lett. 5 (2020) e20016, https://doi.org/10.1002/ael2.20016.
[70] W. Laue, M. Thiemann, E. Scheibler, K.W. Wiegand, Nitrates nitrites 24 (2000) 153–157.
[71] S. Cho, H. Suh, S. Im, G. Kim, M. Kanematsu, S. Morooka, A. Machida, T. Shobu, S. Bae, Characteristic microstructural phase evolution and the compressive strength development mechanisms of tricalcium silicate pastes under various initial carbonation curing environments, Constr. Build. Mater. 409 (2023) 133866, https://doi.org/10.1016/j.conbuildmat.2023.133866.
[72] S. Sim, H. Suh, S. Cho, S. Im, J. Park, J. Liu, S. Bae, Synergistic effects of nano-alumina and triisopropanolamine in Portland limestone cements with various sulfate levels, Cem. Concr. Compos. (2025) 105994, https://doi.org/10.1016/j.cemconcomp.2025.105994.
[73] J. Park, S. Cho, H. Suh, S. Her, J. Yang, S. Bae, Immobilization and leaching behavior of cobalt in alkali-activated fly ash/dehydrated cement paste fine blends, Cem. Concr. Res. 195 (2025) 107921, https://doi.org/10.1016/j.cemconres.2025.107921.
[74] H. Suh, S. Cho, G. Kim, S. Bae, Quantitative characterization of nano-scale pore structures in a consistent volume of cement paste subjected to heating via synchrotron X-ray nanoimaging, Cem. Concr. Res. 185 (2024) 107630, https://doi.org/10.1016/j.cemconres.2024.107630.
[75] L. Li, X. Zhong, T.-C. Ling, Effects of accelerated carbonation and high temperatures exposure on the properties of EAFS and BOFS pressed blocks, J. Build. Eng. 45 (2022) 103504, https://doi.org/10.1016/j.jobe.2021.103504.
[76] X. Zhong, L. Li, Y. Jiang, T.-C. Ling, Elucidating the dominant and interaction effects of temperature, CO2 pressure and carbonation time in carbonating steel slag blocks, Constr. Build. Mater. 302 (2021) 124158, https://doi.org/10.1016/j.conbuildmat.2021.124158.
[77] Z. Tu, M.-z Guo, C.S. Poon, C. Shi, Effects of limestone powder on CaCO3 precipitation in CO2 cured cement pastes, Cem. Concr. Compos. 72 (2016) 9–16, https://doi.org/10.1016/j.cemconcomp.2016.05.019.
[78] X. Wang, H. Luo, F. Zou, J. Cai, Y. Yu, J. Fu, High-Performance CO2 Sequestration Solid Materials Consist of β-C2S and γ-C2S Binary Clinkers Synthesized from Carbide Slag and Sandstone: Sintering, Carbonation, and Microstructure, ACS Sustain. Chem. Eng. 12 (2024) 6840–6855, https://doi.org/10.1021/acssuschemeng.3c05960.
[79] S. Li, X. Du, J. Chang, Investigating the carbonation kinetics of the ternesite-belite-rankinite multi-component carbonatable binder system: Optimizing performance for industrial products, Constr. Build. Mater. 497 (2025) 143883, https://doi.org/10.1016/j.conbuildmat.2025.143883.
[80] M. Tiong, X. Li, K.H. Mo, T.-C. Ling, Effects of moulding pressure and w/c induced pore water saturation on the CO2 curing efficiency of dry-mix cement blocks, Constr. Build. Mater. 335 (2022) 127509, https://doi.org/10.1016/j.conbuildmat.2022.127509.
[81] T. Pei, Y. Wang, D. Zhang, Z. Guo, Z. Chen, W. Meng, S. Cui, Phase composition and structural evolution in water-driven carbonation process of low-calcium Portland cement, Constr. Build. Mater. 504 (2025) 144587, https://doi.org/10.1016/j.conbuildmat.2025.144587.
[82] K. Scrivener, R. Snellings, B. Lothenbach, A practical guide to microstructural analysis of cementitious materials, Crc Press, 2018.
[83] J. Zhang, G.W. Scherer, Comparison of methods for arresting hydration of cement, Cem. Concr. Res. 41 (2011) 1024–1036, https://doi.org/10.1016/j.cemconres.2011.06.003.
[84] S. Her, J. Park, P. Li, S. Bae, Feasibility study on utilization of pulverized eggshell waste as an alternative to limestone in raw materials for Portland cement clinker production, Constr. Build. Mater. 324 (2022) 126589, https://doi.org/10.1016/j.conbuildmat.2022.126589.
[85] P. Li, J. Liu, H. Suh, S. Im, T. Piao, E.Z. Nezhad, K. Wi, S. Bae, Graphene nanoribbons: A novel additive for enhancing the fire resistance of cementitious composites, Constr. Build. Mater. 426 (2024) 136057, https://doi.org/10.1016/j.conbuildmat.2024.136057.
[86] G. Kim, S. Cho, J. Moon, H. Suh, S. Her, S. Sim, S. Bae, Investigation of the hydrate formation and mechanical performance of limestone calcined clay cement paste incorporating nano-CaCO3 and nano-SiO2 as partial limestone substitutes, Constr. Build. Mater. 418 (2024) 135335, https://doi.org/10.1016/j.conbuildmat.2024.135335.
[87] S. Her, J. Park, S. Cho, H. Suh, J. Liu, S. Sim, S. Bae, Synthesis and characterization of MgO- and SrO-doped cement: Mineralogical composition and polymorphism of cement clinker phases, Constr. Build. Mater. 487 (2025) 141994, https://doi.org/10.1016/j.conbuildmat.2025.141994.
[88] J. Yu, S. Sim, H. Song, D. Kim, K. Jang, D. Jeon, S. Cho, J.E. Oh, Examination of sulfate resistance of nano-alumina added ordinary Portland cement paste, focusing on the two different crystallinity of nano-aluminas, Int. J. Concr. Struct. Mater. 17 (2023) 32, https://doi.org/10.1186/s40069-023-00591-7.
[89] Z. Yu, X. Wang, X. Xian, T.-C. Ling, Thermal behavior of carbonated γ-C2S compacts subjected to high temperature: Mechanical properties and phase evolution, Constr. Build. Mater. 451 (2024) 138799, https://doi.org/10.1016/j.conbuildmat.2024.138799.
[90] H. Suh, S. Cho, J. Yang, S. Her, S. Jeong, C.-S. Choi, S. Bae, Analysis of fire-resistance improvement mechanism in low-lime calcium silicate cement paste through nanoscale pore-structure analysis via synchrotron X-ray nanoimaging, Constr. Build. Mater. 475 (2025) 141184, https://doi.org/10.1016/j.conbuildmat.2025.141184.
[91] R. Snellings, A. Bazzoni, K. Scrivener, The existence of amorphous phase in Portland cements: Physical factors affecting Rietveld quantitative phase analysis, Cem. Concr. Res. 59 (2014) 139–146, https://doi.org/10.1016/j.cemconres.2014.03.002.
[92] S. Regalla, N. Senthil Kumar, Experimental investigations on performance efficiency characteristics of ultra-high-performance concrete (UHPC) with enhanced sustainable mineral admixtures 10 (2025) 2538978, https://doi.org/10.1080/24705314.2025.2538978.
[93] H. Kang, J. Lee, J.-B. Park, J. Moon, Investigation on the Micro-Grinding Induced Crystallographic Variations of Nine Different Clinkers, Int. J. Concr. Struct. Mater. 18 (2024) 23, https://doi.org/10.1186/s40069-024-00660-5.
[94] B. Lu, Z. Huo, Q. Xu, G. Hou, X. Wang, J. Liu, X. Hu, Characteristics of CSH under carbonation and its effects on the hydration and microstructure of cement paste, Constr. Build. Mater. 364 (2023) 129952, https://doi.org/10.1016/j.conbuildmat.2022.129952.
[95] S. Bae, R. Taylor, D. Kilcoyne, J. Moon, P.J.M. Monteiro, Effects of Incorporating High-Volume Fly Ash into Tricalcium Silicate on the Degree of Silicate Polymerization and Aluminum Substitution for Silicon in Calcium Silicate Hydrate, Materials 10 (2017), https://doi.org/10.3390/ma10020131.
[96] Rune Wittendorff M. Jensen, J. Skibsted, Aqueous Carbonation of Calcium Silicates With Different Ca/Si Ratios Studied by Solid-State NMR Spectroscopy, Magn. Reson. Chem. 63 (2025) 476–494, https://doi.org/10.1002/mrc.5528.
[97] A. Khawam, D.R. Flanagan, Solid-State Kinetic Models: Basics and Mathematical Fundamentals, J. Phys. Chem. B. 110 (2006) 17315–17328, https://doi.org/10.1021/jp062746a.
[98] W. Ashraf, J. Olek, Carbonation activated binders from pure calcium silicates: Reaction kinetics and performance controlling factors, Cem. Concr. Compos. 93 (2018) 85–98, https://doi.org/10.1016/j.cemconcomp.2018.07.004.
[99] C.J. Goodbrake, J.F. Young, R.L. Berger, Reaction of Beta-Dicalcium Silicate and Tricalcium Silicate with Carbon Dioxide and Water Vapor, J. Am. Ceram. Soc. 62 (1979) 168–171, https://doi.org/10.1111/j.1151-2916.1979.tb19046.x.
[100] T. Wang, Z. Yi, R. Guo, H. Huang, S. Garcia, M.M. Maroto-Valer, Particle carbonation kinetics models and activation methods under mild environment: The case of calcium silicate, Chem. Eng. J. 423 (2021) 130157, https://doi.org/10.1016/j.cej.2021.130157.
[101] V. Thiery, E. Dubois, S. Bellayer, The good, the bad and the ugly polishing: Effect of abrasive size on standardless EDS analysis of Portland cement clinker's calcium silicates, Micron 158 (2022) 103266, https://doi.org/10.1016/j.micron.2022.103266.

[102] J. Lim, H. Kim, S.Y. Park, Hard X-ray nanotomography beamline 7C XNI at PLS-II, J. Synchrotron Radiat. 21 (2014) 827–831, https://doi.org/10.1107/S1600577514008224.
[103] M. Dierick, B. Masschaele, L.Van Hoorebeke, Octopus, a fast and user-friendly tomographic reconstruction package developed in LabView (R), Meas. Sci. Technol. 15 (2004) 1366–1370, https://doi.org/10.1088/0957-0233/15/7/020.
[104] P. Westenberger, Avizo—Three-Dimensional Visualization Framework, Geoinformatics 2008Data Knowl. (2008) 13–14.
[105] Y. Chen, Y. Ning, X. Chen, W. Xuan, Y. Guo, Experimental Investigation on the Effect of Curing Condition and Admixture on Meso-Structure of Recycled Aggregate Concrete Based on X-ray CT, Int. J. Concr. Struct. Mater. 17 (2023) 11, https://doi.org/10.1186/s40069-022-00572-2.
[106] C. Ruan, J. Lin, S. Chen, K. Sagoe-Crentsil, W. Duan, Effect of Graphene Oxide on the Pore Structure of Cement Paste: Implications for Performance Enhancement, Acs. Appl. Nano. Mater. 4 (2021) 10623–10633, https://doi.org/10.1021/acsanm.1c02090.
[107] J. Segurado, J. Llorca, Computational micromechanics of composites: The effect of particle spatial distribution, Mech. Mater. 38 (2006) 873–883, https://doi.org/10.1016/j.mechmat.2005.06.026.
[108] H. Suh, S. Cho, S. Her, S. Bae, Influence of multi-scale three-dimensional pore characteristics on the mechanical properties of graphene oxide and carbon nanotube incorporated cement paste, Cem. Concr. Res. 174 (2023) 107326, https://doi.org/10.1016/j.cemconres.2023.107326.
[109] H. Suh, S. Cho, S. Im, J. Moon, J. Park, J. Lim, E.Z. Nezhad, S. Seok, B.-I. Bae, S. Bae, Characterization of thermal resistance and mechanical strength recovery of carbon nanotubes incorporated Portland cement composites subjected to heating and rehydration: Visualization of pore structural evolutions via synchrotron 3D X-ray nanoimaging, Cem. Concr. Compos. 146 (2024) 105361, https://doi.org/10.1016/j.cemconcomp.2023.105361.
[110] H. Suh, G. Kim, S. Cho, P. Li, D.-H. Son, D. Koo, J. Lim, C.-S. Choi, S. Seok, S. Bae, Comparative analysis of the synergistic effects of hybrid nanomaterial reinforcement in cementitious Composites: A perspective for pore refinement and thermal resistance, Constr. Build. Mater. 401 (2023) 132856, https://doi.org/10.1016/j.conbuildmat.2023.132856.
[111] H. Suh, G. Kim, S. Im, J. Park, S. Bae, A mechanism study of thermal resistance formation and post-fire strength recovery in cement paste with carbon nanotubes and nanosilica via focused ion beam/scanning electron microscopy tomography, J. Build. Eng. 97 (2024) 110750, https://doi.org/10.1016/j.jobe.2024.110750.
[112] T. Zingg, ETH Zürich, Beitrag Zur. Schotteranalyse (1935), https://doi.org/10.3929/ethz-a-000103455.
[113] H. Liu, C. Lv, S. Zhao, Z. Liu, Y. Zheng, F. Wang, Ion-doped γ-C2S: Clinker characteristics, carbonation products, and carbonation properties, Constr. Build. Mater. 438 (2024) 137033, https://doi.org/10.1016/j.conbuildmat.2024.137033.
[114] S. Liu, L. Zhang, D. Xuan, P. Shen, J. Zhu, X. Guan, C. Shi, Enhanced carbonation reactivity of wollastonite by rapid cooling process: Towards an ultra-low calcium CO2 sequestration binder, Constr. Build. Mater. 299 (2021) 124336, https://doi.org/10.1016/j.conbuildmat.2021.124336.
[115] H. Wang, D. Ma, J. Zhang, W. Song, S. Liu, X. Guan, Y. Bian, J. Zhu, Research on the method of improving carbon storage capacity of a new low calcium CO2 storage binder: Based on the recycling of heavy metal Ba ions, J. Mater. Res. Technol. 33 (2024) 1872–1882, https://doi.org/10.1016/j.jmrt.2024.09.083.
[116] Y. Yang, Y. Lai, K. Wu, W. Wang, J. Fang, Y. Gao, Z. Yang, Effect of Cr2O3 on the clinkerization and carbonation properties of γ-C2S, J. Build. Eng. 90 (2024) 109395, https://doi.org/10.1016/j.jobe.2024.109395.
[117] Y. Yang, Y. Lai, L. Xu, W. Wang, J. Fang, Q. Yuan, K. Wu, Z. Yang, Effect of ZnO on the clinkerization and carbonation behavior of γ-C2S, Sustain. Mater. Technol. 40 (2024) e00945, https://doi.org/10.1016/j.susmat.2024.e00945.
[118] J. Zhu, J. Cao, H. Wang, Y. Bian, Probe into the substitution preference of zinc ions and the mechanism of its influence on the carbonation properties of Low Calcium Carbonatable Binder, Constr. Build. Mater. 489 (2025) 142123, https://doi.org/10.1016/j.conbuildmat.2025.142123.
[119] J. Zhu, D. Ma, S. Liu, X. Guan, S.P. Shah, The influence of nano-SiO2 on the carbonation properties of low calcium CO2 sequestration binder and its mechanism, Constr. Build. Mater. 416 (2024) 135124, https://doi.org/10.1016/j.conbuildmat.2024.135124.
[120] Y. Tanigawa, K. Yamada, Size effect in compressive strength of concrete, Cem. Concr. Res. 8 (1978) 181–190, https://doi.org/10.1016/0008-8846(78)90007-8.
[121] M.E. Sastre de Vicente, The Concept of Ionic Strength Eighty Years after Its Introduction in Chemistry, J. Chem. Educ. 81 (2004) 750, https://doi.org/10.1021/ed081p750.
[122] G.N. Lewis, M. Randall, Thermodynamics, Courier Dover Publications, 2020.
[123] T. Solomon, The Definition and Unit of Ionic Strength, J. Chem. Educ. 78 (2001) 1691, https://doi.org/10.1021/ed078p1691.
[124] P. Ayogu, M. Ezugwu, F. Eze, Principle of Common-ion Effect and its Application in Chemistry: a Review, J. Chem. Lett. 1 (2020) 77–83, https://doi.org/10.22034/jchemlett.2020.113421.
[125] I.R. Ariyarathna, E. Miliordos, Geometric and electronic structure analysis of calcium water complexes with one and two solvation shells, Phys. Chem. Chem. Phys. 22 (2020) 22426–22435, https://doi.org/10.1039/D0CP04309E.
[126] D.R. Lide, CRC handbook of chemistry and physics: a ready-reference book of chemical and physical data, CRC press, 1995.
[127] B. Kutus, A. Gácsi, A. Pallagi, I. Pálinkó, G. Peintler, P. Sipos, A comprehensive study on the dominant formation of the dissolved Ca(OH)2(aq) in strongly alkaline solutions saturated by Ca(ii), RSC Adv. 6 (2016) 45231–45240, https://doi.org/10.1039/c6ra05337h.
[128] H. Suh, H. Jee, J. Kim, R. Kitagaki, S. Ohki, S. Woo, K. Jeong, S. Bae, Influences of rehydration conditions on the mechanical and atomic structural recovery characteristics of Portland cement paste exposed to elevated temperatures, Constr. Build. Mater. 235 (2020) 117453, https://doi.org/10.1016/j.conbuildmat.2019.117453.
[129] H. Suh, S. Im, J. Kim, S. Bae, Instant mechanical recovery of heat-damaged nanosilica-incorporated cement composites under various rehydrations procedures, Mater. Struct. 55 (2021) 5, https://doi.org/10.1617/s11527-021-01847-y.
[130] A. Carrico, J.A. Bogas, M. Guedes, Thermoactivated cementitious materials–A review, Constr. Build. Mater. 250 (2020) 118873, https://doi.org/10.1016/j.conbuildmat.2020.118873.
[131] A.H.B. Dourado, Electric Double Layer: The Good, the Bad, and the Beauty, Electrochem 3 (2022) 789–808, https://doi.org/10.3390/electrochem3040052.
[132] S. Chatterji, M. Kawamura, Electrical double layer, ion transport and reactions in hardened cement paste, Cem. Concr. Res. 22 (1992) 774–782, https://doi.org/10.1016/0008-8846(92)90101-Z.
[133] W. Li, Z. Sun, Second Hydration Shell of Mg2+: Competition between Ion–Water Interaction and Hydrogen Bonding Interaction, J. Phys. Chem. Lett. 16 (2025) 503–509, https://doi.org/10.1021/acs.jpclett.4c02771.
[134] B. Das, A. Chandra, Ab Initio Molecular Dynamics Study of Aqueous Solutions of Magnesium and Calcium Nitrates: Hydration Shell Structure, Dynamics and Vibrational Echo Spectroscopy, J. Phys. Chem. Lett. 126 (2022) 528–544, https://doi.org/10.1021/acs.jpcb.1c08545.
[135] M. Santoro, F. Gorelli, J. Haines, O. Cambon, C. Levelut, G. Garbarino, Silicon carbonate phase formed from carbon dioxide and silica under pressure, Proc. Natl. Acad. Sci. 108 (2011) 7689–7692, https://doi.org/10.1073/pnas.1019691108.
[136] X. Yong, J.S. Tse, J. Chen, Mechanism of Chemical Reactions between SiO2 and CO2 under Mantle Conditions, ACS Earth Space Chem. 2 (2018) 548–555, https://doi.org/10.1021/acsearthspacechem.7b00144.
[137] C. Chen, H. Zhong, X. Wang, M. Ning, X. Wang, Y. Ge, H. Wang, R. Tang, M. Hou, Thermodynamic and Kinetic Studies of Dolomite Formation: A Review, Minerals 13 (2023) 1479, https://doi.org/10.3390/min13121479.
[138] K.B. Krauskopf, D.K. Bird, Introduction to geochemistry, McGraw-Hill, New York, 1995.
[139] Y. Mu, Z. Liu, F. Wang, X. Huang, Effect of barium doping on carbonation behavior of γ-C2S, J. CO2. Util. 27 (2018) 405–413, https://doi.org/10.1016/j.jcou.2018.08.018.
[140] L. Cheng, Y. Chen, T. Liu, H.J.H. Brouwers, Q. Yu, Understanding the CaCO3 phase transition of carbonated wollastonite composites caused by sodium tripolyphosphate: From amorphous to crystalline, Cem. Concr. Compos. 148 (2024) 105477, https://doi.org/10.1016/j.cemconcomp.2024.105477.
[141] D. Wang, C. Xiong, W.Z. Li, J. Chang, Growth of Calcium Carbonate Induced by Accelerated Carbonation of Tricalcium Silicate, ACS Sustain. Chem. Eng. 8 (2020) 14718–14731, https://doi.org/10.1021/acssuschemeng.0c02260.
[142] X. Liu, P. Feng, Y. Cai, X. Yu, C. Yu, Q. Ran, Carbonation behavior of calcium silicate hydrate (C-S-H): Its potential for CO2 capture, Chem. Eng. J. 431 (2022) 134243, https://doi.org/10.1016/j.cej.2021.134243.
[143] G.W. Groves, A. Brough, I.G. Richardson, C.M. Dobson, Progressive Changes in the Structure of Hardened C3S Cement Pastes Due to Carbonation, J. Am. Ceram. Soc. 74 (1991) 2891–2896, https://doi.org/10.1111/j.1151-2916.1991.tb06859.x.
[144] T.F. Sevelsted, J. Skibsted, Carbonation of C–S–H and C–A–S–H samples studied by 13C, 27Al and 29Si MAS NMR spectroscopy, Cem. Concr. Res. 71 (2015) 56–65, https://doi.org/10.1016/j.cemconres.2015.01.019.
[145] P. Liu, M. Zhang, L. Mo, J. Zhong, M. Xu, M. Deng, Probe into carbonation mechanism of steel slag via FIB-TEM: The roles of various mineral phases, Cem. Concr. Res. 162 (2022) 106991, https://doi.org/10.1016/j.cemconres.2022.106991.
[146] G. Kim, S. Im, H. Jee, H. Suh, S. Cho, M. Kanematsu, S. Morooka, T. Koyama, Y. Nishio, A. Machida, Effect of magnesium silicate hydrate (MSH) formation on the local atomic arrangements and mechanical properties of calcium silicate hydrate (CSH): In situ X-ray scattering study, Cem. Concr. Res. 159 (2022) 106869, https://doi.org/10.1016/j.cemconres.2022.106869.
[147] J. Sun, M.F. Bertos, S.J.R. Simons, Kinetic study of accelerated carbonation of municipal solid waste incinerator air pollution control residues for sequestration of flue gas CO2, Energy Environ. Sci. 1 (2008) 370–377, https://doi.org/10.1039/B804165M.
[148] H. Zhang, J. Chen, R. Shao, Q. Zhang, B. Lu, G. Xia, G. Hou, Z. Yun, The usage of rankinite for carbon capture and storage and carbonation kinetics, Energy Sources Part. A-Recovery Util. Environ. Eff. 40 (2018) 1629–1646, https://doi.org/10.1080/15567036.2018.1486484.
[149] J. Pae, N. Lee, J. Moon, Effect of curing temperature on the carbonation kinetics, microstructure, and mechanical properties of CO2-cured pseudowollastonite, Cem. Concr. Compos. 167 (2026) 106441, https://doi.org/10.1016/j.cemconcomp.2025.106441.
[150] E.A. Giess, Equations and Tables for Analyzing Solid-state Reaction Kinetics, J. Am. Ceram. Soc. 46 (1963) 374–376, https://doi.org/10.1111/j.1151-2916.1963.tb11754.x.
[151] P.W. Voorhees, The theory of Ostwald ripening, J. Stat. Phys. 38 (1985) 231–252, https://doi.org/10.1007/BF01017860.
[152] X. Liu, P. Tang, W. Chen, Development of an ettringite-based low carbon binder by promoting the nucleation and Ostwald ripening process, Constr. Build. Mater. 427 (2024) 136282, https://doi.org/10.1016/j.conbuildmat.2024.136282.

[153] Y.-Y. Kim, A.S. Schenk, J. Ihli, A.N. Kulak, N.B.J. Hetherington, C.C. Tang, W. W. Schmahl, E. Griesshaber, G. Hyett, F.C. Meldrum, A critical analysis of calcium carbonate mesocrystals, Nat. Comm. 5 (2014) 4341, https://doi.org/10.1038/ncomms5341.
[154] A.E. Morandeau, C.E. White, Role of magnesium-stabilized amorphous calcium carbonate in mitigating the extent of carbonation in alkali-activated slag, Chem. Mater. 27 (2015) 6625–6634, https://doi.org/10.1021/acs.chemmater.5b02382.
[155] Y.-M. Ju, F. Huang, X. Ding, L.-B. Mao, S.-H. Yu, Phase transformation-induced Mg isotope fractionation in Mg-mediated CaCO3 mineralization, Nano. Res. 16 (2023) 3597–3602, https://doi.org/10.1007/s12274-022-5171-z.
[156] J.M. Koehler, N. Visaveliya, A. Knauer, Controlling formation and assembling of nanoparticles by control of electrical charging, polarization, and electrochemical potential, Nanotechol. Rev. 3 (2014) 553–568, https://doi.org/10.1515/ntrev-2014-0006.
[157] D. Gebauer, How Can Additives Control the Early Stages of Mineralisation? Minerals 8 (2018) 179, https://doi.org/10.3390/min8050179.
[158] J. Polte, Fundamental growth principles of colloidal metal nanoparticles – a new perspective, Cryst. Eng. Comm. 17 (2015) 6809–6830, https://doi.org/10.1039/C5CE01014D.
[159] A.S. Perelson, Spatial distribution of surface immunoglobulin on B lymphocytes: Local ordering, Exp. Cell. Res. 112 (1978) 309–321, https://doi.org/10.1016/0014-4827(78)90214-8.
[160] N.K. Bui, R. Kurihara, M. Kanematsu, H. Hyodo, T. Noguchi, I. Maruyama, Effect of temperature on binding process of calcium carbonate concrete through aragonite crystals precipitation, Compos. B Eng. 283 (2024) 111625, https://doi.org/10.1016/j.compositesb.2024.111625.
[161] S. Nie, J. Zhou, F. Yang, M. Lan, J. Li, Z. Zhang, Z. Chen, M. Xu, H. Li, J. G. Sanjayan, Analysis of theoretical carbon dioxide emissions from cement production: Methodology and application, J. Clean. Prod. 334 (2022) 130270, https://doi.org/10.1016/j.jclepro.2021.130270.
[162] K.-H. Yang, Y.-B. Jung, M.-S. Cho, S.-H. Tae, Effect of supplementary cementitious materials on reduction of CO2 emissions from concrete, J. Clean. Prod. 103 (2015) 774–783, https://doi.org/10.1016/j.jclepro.2014.03.018.
[163] F. Brentrup, J. Lammel, T. Stephani, B. Christensen, Updated carbon footprint values for mineral fertilizer from different world regions, 17-19.
[164] J.A. Silva, Inorganic fertilizer materials. (2000) 117-120.
[165] D.A. Sabella, N. Dyah Ayu Nyata, S. Sintha Soraya, Suprihatin, P. Caecilia, Production of Calcium Nitrate Fertilizer from Calcium Hydroxide Waste: Effects of Reaction Temperature and Nitric Acid Concentration 10 (2026) 584–591, https://doi.org/10.29165/ajarcde.v10i2.1110.
[166] Y. Xie, C. Qian, Improved ettringite stabilization by calcium carbonate and calcium nitrate additions in ternary PC-CSA-C$ systems, Cem. Concr. Res. 175 (2024) 107383, https://doi.org/10.1016/j.cemconres.2023.107383.
[167] L. Lu, X. Liu, J. Wang, S. Wang, Y. Yao, Y. Xu, M. Jiang, Y. Xiao, Y. Li, Z. Wang, S. Cui, Effect of nitrate anions on sulfate balance and hydration kinetics in C3S/C3A systems, Cem. Concr. Res. 198 (2025) 108008, https://doi.org/10.1016/j.cemconres.2025.108008.
[168] H. Justnes, E.C. Nygaard, Technical calcium nitrate as set accelerator for cement at low temperatures, Cem. Concr. Res. 25 (1995) 1766–1774, https://doi.org/10.1016/0008-8846(95)00172-7.
[169] M. Balonis, M. Mędala, F.P. Glasser, Influence of calcium nitrate and nitrite on the constitution of AFm and AFt cement hydrates, Adv. Cem. Res. 23 (2011) 129–143, https://doi.org/10.1680/adcr.10.00002.